

Manuscript Number:

Title: LiCaFeF₆: A zero-strain cathode material for use in Li-ion batteries

Article Type: Research Paper

Keywords: Lithium-ion battery; cathode material; zero-strain; lithium metal fluoride; Li insertion

Corresponding Author: Dr. Lea de Biasi,

Corresponding Author's Institution: Karlsruhe Institute of Technology

First Author: Lea de Biasi

Order of Authors: Lea de Biasi; Georg Lieser; Christoph Dräger; Sylvio Indris; Jatinkumar Rana; Gerhad Schumacher; Reiner Mönig; Helmut Ehrenberg; Joachim R. Binder; Holger geßwein

Manuscript Region of Origin: GERMANY

Abstract: A new zero-strain LiCaFeF₆ cathode material for reversible insertion and extraction of lithium ions is presented. LiCaFeF₆ is synthesized by a solid-state reaction and processed to a conductive electrode composite via high-energy ball-milling. In the first cycle, a discharge capacity of 112 mAh g⁻¹ is achieved in the voltage range from 2.0 V to 4.5 V. The electrochemically active redox couple is Fe³⁺/Fe²⁺ as confirmed by Mössbauer spectroscopy and X-ray absorption spectroscopy. The compound has a trigonal colquiriite-type crystal structure (space group P3̄1c). By means of in situ and ex situ XRD as well as X-ray absorption fine structure spectroscopy a reversible response to Li uptake/release is found. For an uptake of 0.8 mole Li per formula unit only minimal changes occur in the lattice parameters causing a total change in unit cell volume of less than 0.5 %. The spatial distribution of cations in the crystal structure as well as the linkage between their corresponding fluorine octahedra is responsible for this very small structural response. With its zero-strain behaviour this material is expected to exhibit only negligible mechanical degradation. It may be used as a cathode material in future lithium-ion batteries with strongly improved safety and cycle life.

May 30, 2017

Dear Editor and Referees,

I am enclosing herewith an article manuscript entitled “LiCaFeF₆: A zero-strain cathode material for use in Li-ion batteries” by L. de Biasi *et al.* for publication in Journal of Power Sources.

One major drawback of current lithium-ion batteries is that most electrode materials experience mechanical stresses during electrochemical cycling due to strain associated with phase transitions and lattice parameter changes upon Li uptake and release. In order to minimize mechanical defects, so-called “zero-strain” materials are of interest due to their negligibly small changes in lattice parameters and, hence, smaller lattice strain during cycling, which is promising for a long cycle life. The most common zero-strain lithium insertion material is the spinel-type anode Li₄Ti₅O₁₂ (LTO). The volume change of this material is merely 0.2 %. To our knowledge, an employable positive electrode material for Li-ion batteries with zero-strain properties is not known yet. The volume changes observed for commercial cathode materials are, for example, ~ 6.5 % for LiMn₂O₄ and ~ 7.0 % for LiFePO₄.

The material presented here belongs to a novel group of compounds, that are quaternary lithium transition metal fluorides, which could be possible future candidates for cathode applications in lithium-ion batteries (Lieser *et al.*, 2014; de Biasi *et al.* 2015; Lieser *et al.* 2015). In this study, we show that the colquiriite-type crystal structure of LiCaFeF₆ has a favorable cation arrangement and exhibits unprecedented low strains for a cathode material and a volume change of less than 0.5 % during cycling.

We present an analysis of the chemical, structural and electrochemical properties of LiCaFeF₆ cathode material. Therefore, data from *in situ* and *ex situ* X-ray diffraction, X-ray absorption spectroscopy, Mössbauer, and NMR spectroscopy are used to elucidate the lithium insertion mechanism and the induced zero-strain behavior of this material.

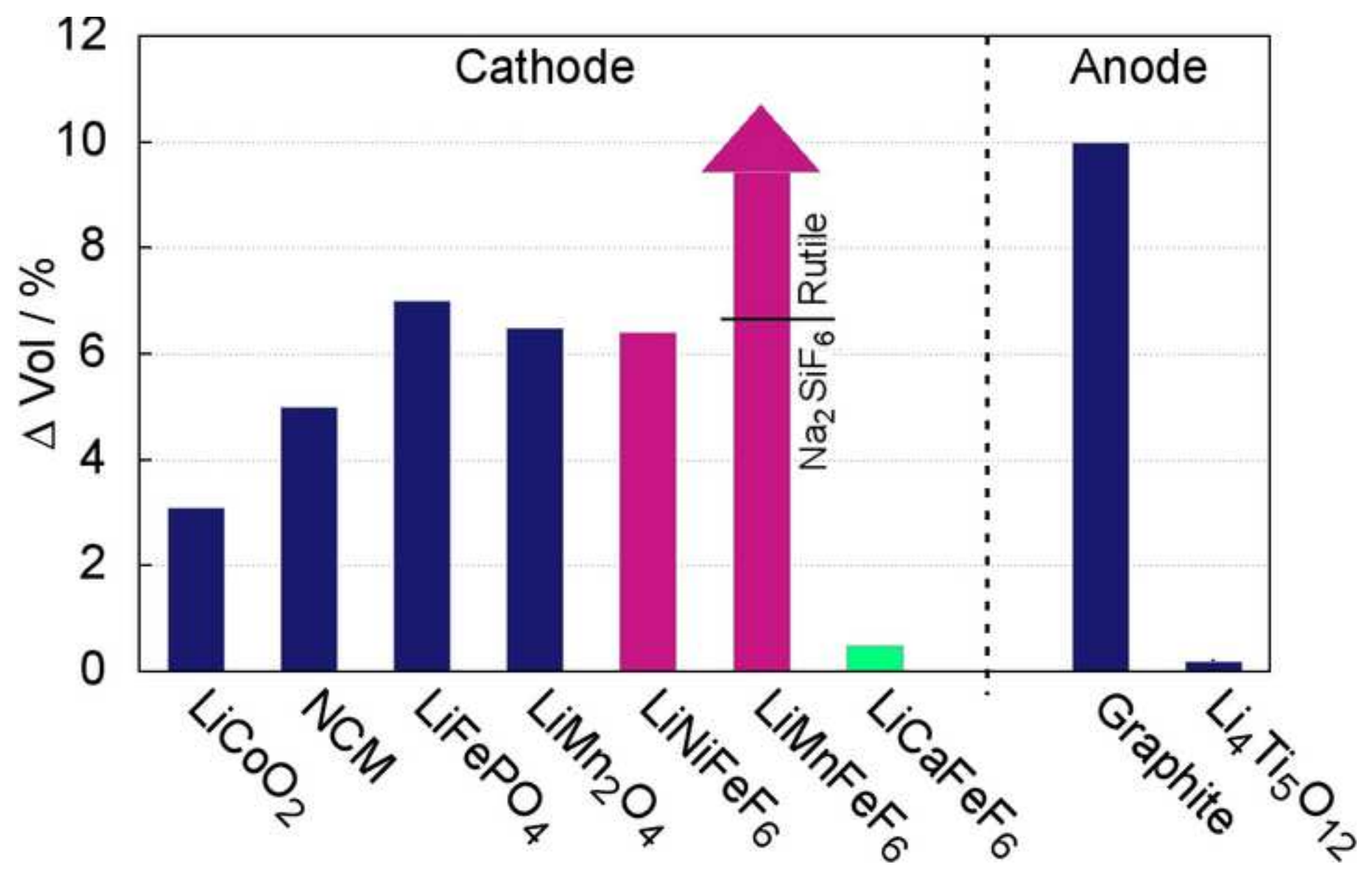
Up to now, no other commercially used cathode material for Li-ion batteries with comparable properties is known, which makes LiCaFeF₆ a promising candidate for future energy storage applications.

We are sure that this subject is of strong interest and with the attention to detail in data evaluation and a high scientific integrity we believe that this work can meet the high level of Journal of Power Sources. We assure you that the work has not been submitted previously to your journal, that it has not been published previously, is not under consideration for publication elsewhere, and is approved by all authors and host authorities.

I am looking forward to your feedback.

Sincerely,

Lea de Biasi



*Highlights (for review)

- $\text{Li}_{1+x}\text{CaFeF}_6$ shows a unit cell volume change of $< 0.5\%$ during Li insertion ($x=0.8$).
- The zero-strain properties are unique among commercial LIB cathode materials.
- Reversibility of structural changes and long-term stability were confirmed by XAS.
- The electrochemically active redox couple is $\text{Fe}^{3+}/\text{Fe}^{2+}$.

LiCaFeF₆: A zero-strain cathode material for use in Li-ion batteries

1
2
3
4
5 Lea de Biasi^{1,2,3}, Georg Lieser¹, Christoph Dräger¹, Sylvio Indris¹, Jatinkumar Rana^{4,5},
6
7 Gerhard Schumacher⁴, Reiner Mönig^{1,2}, Helmut Ehrenberg^{1,2}, Joachim R. Binder¹, Holger
8
9 Geßwein^{1,2}
10

11
12
13
14
15
16 ¹Institute for Applied Materials, Karlsruhe Institute of Technology (KIT), 76344 Eggenstein-
17
18 Leopoldshafen, Germany; ²Helmholtz Institute Ulm (HIU), 89069 Ulm, Germany; ³Institute
19
20 of Nanotechnology, Karlsruhe Institute of Technology (KIT), 76344 Eggenstein-
21
22 Leopoldshafen, Germany; ⁴Helmholtz-Zentrum Berlin für Materialien und Energie, Hahn-
23
24 Meitner-Platz 1, 14109 Berlin, Germany; ⁵Binghamton University, Department of Physics,
25
26 Applied Physics and Astronomy, 4400 Vestal Parkway, Vestal, NY.
27
28
29
30

Abstract

31
32
33
34
35 A new zero-strain LiCaFeF₆ cathode material for reversible insertion and extraction of
36
37 lithium ions is presented. LiCaFeF₆ is synthesized by a solid-state reaction and processed to a
38
39 conductive electrode composite via high-energy ball-milling. In the first cycle, a discharge
40
41 capacity of 112 mAh g⁻¹ is achieved in the voltage range from 2.0 V to 4.5 V. The
42
43 electrochemically active redox couple is Fe³⁺/Fe²⁺ as confirmed by Mössbauer spectroscopy
44
45 and X-ray absorption spectroscopy. The compound has a trigonal colquiriite-type crystal
46
47 structure (space group $P\bar{3}1c$). By means of *in situ* and *ex situ* XRD as well as X-ray
48
49 absorption fine structure spectroscopy a reversible response to Li uptake/release is found. For
50
51 an uptake of 0.8 mole Li per formula unit only minimal changes occur in the lattice
52
53 parameters causing a total change in unit cell volume of less than 0.5 %. The spatial
54
55 distribution of cations in the crystal structure as well as the linkage between their
56
57
58
59
60
61
62
63
64
65

1 corresponding fluorine octahedra is responsible for this very small structural response. With
2 its zero-strain behaviour this material is expected to exhibit only negligible mechanical
3 degradation. It may be used as a cathode material in future lithium-ion batteries with strongly
4 improved safety and cycle life.
5
6
7

8
9 **Keywords:** Lithium-ion battery; cathode material; zero-strain; lithium metal fluoride; Li
10 insertion
11
12
13

14 15 16 17 **1. Introduction**

18
19 The constantly growing market of power-driven devices requires improved energy
20 storage technologies. Lithium-ion batteries (LIB) have become the prevalent storage system
21 in electronic devices and are of increasing importance in electric vehicles as well as in
22 stationary energy storage systems. Although being widespread in the market, in many cases,
23 the lifetime of LIB leaves to be desired. One major drawback is that most electrode materials
24 experience mechanical stresses during electrochemical cycling due to strain associated with
25 phase transitions and lattice parameter changes upon Li uptake and release. For example, the
26 volume changes observed for commercial cathode materials are $\sim 6.5\%$ [1,2] for LiMn_2O_4
27 and $\sim 7.0\%$ [3,4] for LiFePO_4 . During cycling, a mismatch in the lattice parameters at phase
28 boundaries between domains of coexisting phases can lead to discontinuous lattice strain
29 which leads to mechanical stresses that can lead to crack nucleation and growth. Such
30 mechanical defects are barriers for electronic and ionic transport and have been associated
31 with capacity fading [5–7]. In order to achieve batteries with high cycle life, rigid coatings
32 have been applied to LiCoO_2 electrode particles to minimized mechanical effects [8,9]. But it
33 was shown that the crystal structure of coated LiCoO_2 still expands and contracts exactly the
34 same way as that of uncoated material [10].
35
36
37
38
39
40
41
42
43
44
45
46
47
48
49
50
51
52
53
54
55
56

57
58 In order to minimize mechanical defects also new materials have been investigated.
59 The so-called “zero-strain” materials [11] are of interest due to their negligibly small changes
60
61
62
63
64
65

1 in lattice parameters and, hence, smaller lattice strain at phase boundaries during cycling,
2 which is promising for a long cycle life. The most common zero-strain lithium insertion
3 material is the spinel-type anode $\text{Li}_4\text{Ti}_5\text{O}_{12}$. Upon cycling 3 Li^+ ions can be transferred per
4 formula unit. Although this process is accompanied by a two-phase transition, the volume
5 change of this anode material is merely 0.2 % [12]. A comparable zero-strain effect was
6 evidenced for the positive electrode material $\text{Li}_{1+x}\text{Rh}_2\text{O}_4$, which also has a spinel-type crystal
7 structure [13,14]. Nevertheless, rhodium is an expensive element making this material rather
8 unattractive for application. To our knowledge an employable positive electrode material for
9 Li-ion batteries with zero-strain properties is not known yet.

21 The material presented here belongs to a novel group of compounds, that are
22 quaternary lithium transition metal fluorides with formula $\text{AM}^{\text{II}}\text{M}^{\text{III}}\text{F}_6$ [15–18]. A close
23 packed arrangement of fluorine anions forms the basis of their crystalline structure. According
24 to the ratio of ionic radii of the different valent metal cations A, M^{II} , and M^{III} various cationic
25 arrangements in an octahedral coordination are possible resulting in the three structure types,
26 the trirutile-type ($P4_2/mnm$), the Na_2SiF_6 -type ($P321$), and the colquiriite type ($P\bar{3}1c$)
27 structure[19]. The electrochemical properties of trirutile-type (LiNiFeF_6 [15,16,18,20],
28 LiMgFeF_6 [20,21], LiCoFeF_6 [20]) and Na_2SiF_6 -type compounds (LiMnFeF_6 [17]) were
29 studied recently. Furthermore, the lithium insertion mechanisms of the trirutile-type host
30 structures of LiFe_2F_6 [15] and LiNiFeF_6 [18] were investigated by *in situ* X-ray diffraction.
31 Both, LiNiFeF_6 and LiMnFeF_6 show good electrochemical performance with a reversible
32 specific capacity of 88 mAh g^{-1} and 95 mAh g^{-1} . However, the volume expansion of the unit
33 cells upon lithium insertion is 6 % for trirutile-type LiNiFeF_6 [18] and 6.5 % for Na_2SiF_6 -type
34 LiMnFeF_6 [17]. Moreover, for LiMnFeF_6 material a cation site exchange and partial
35 transformation into rutile-type arrangement was detected by *ex situ* XRD [17], which is
36 accompanied by a massive volume expansion.

1
2 In this study, we show that the colquiriite-type crystal structure of LiCaFeF₆ has a
3 favourable cation arrangement and exhibits unprecedented low strains for a cathode. We
4 present an analysis of the chemical, structural and electrochemical properties of LiCaFeF₆
5 cathode material. Therefore, data from *in situ* and *ex situ* X-ray diffraction, X-ray absorption
6 spectroscopy, Mössbauer, and NMR spectroscopy are used to elucidate the lithium insertion
7 mechanism and the induced zero-strain behaviour of this material.
8
9
10
11
12
13
14
15
16

17 **2. Experimental**

18 **2.1. Synthesis and preparation of cathode films**

19
20
21 LiCaFeF₆ was prepared by a solid-state reaction as described by Viebahn [19]. Prior to
22 synthesis, FeF₃ was pre-dried at 350 °C. Then, stoichiometric amounts of LiF, CaF₂, and FeF₃
23 were thoroughly homogenized in a mortar under inert Ar atmosphere in a glovebox. The
24 mixture was heated to 650 °C for 10 hours in an Ar-filled Cu ampoule at a heating rate of 5
25 °C min⁻¹ yielding to the formation of the LiCaFeF₆ powder. In order to obtain a conductive
26 composite with good electrochemical performance, 2.7 g of the as-prepared LiCaFeF₆ was
27 processed by mechanical milling with carbon (Super C65, Timcal) and PvdF binder (KYNAR
28 Powerflex LBG-1, Arkema) at a ratio of 72 wt.-% / 25 wt.-% / 3 wt.-%. The milling was
29 performed under dry conditions in air using a planetary ball mill (Pulverisette 5, Fritsch) with
30 milling balls (100 g, 3 mm diameter) and an 80 mL milling chamber both made of yttria-
31 stabilized zirconia. To prepare cathode films, the LiCaFeF₆ composite was dispersed in N-
32 methyl-2-pyrrolidone to form a homogeneous slurry. A thin film of the slurry was cast on 12
33 mm diameter aluminium current collectors and dried in an oven at 80 °C for 24 hours.
34
35
36
37
38
39
40
41
42
43
44
45
46
47
48
49
50
51
52
53
54
55

56 **2.2. Chemical and structural characterisation**

57
58 The morphology and crystal structure of the as-synthesized sample as well as of the
59 ball-milled composite were characterized by scanning electron microscopy and X-ray powder
60
61
62
63
64
65

1
2
3
4
5
6
7
8
9
10
11
12
13
14
15
16
17
18
19
20
21
22
23
24
25
26
27
28
29
30
31
32
33
34
35
36
37
38
39
40
41
42
43
44
45
46
47
48
49
50
51
52
53
54
55
56
57
58
59
60
61
62
63
64
65

diffraction. SEM images were recorded using a Zeiss Supra 55 microscope. XRD patterns were acquired with a Siemens D5000 diffractometer equipped with a copper tube ($\lambda = 1.54184 \text{ \AA}$) and a detector using energy discrimination. Measurements were conducted in the $10\text{--}120^\circ$ 2θ angular range with increments of 0.04° in 2θ at a constant counting time of 12 s (divergence slit = 1° , anti-scatter slit = 1°). Analyses of the XRD data were performed by use of the Rietveld method with the software TOPAS version 5 (Bruker AXS). The instrumental profile shape was determined using the fundamental parameter approach [22]. Sample broadening effects of the synthesized materials, such as the apparent crystallite size and microstrain, were accounted for by convolution-based profile fitting as implemented in the TOPAS programme. This approach is equivalent to the Double-Voigt method described by Balzar [23,24] and is based on the integral breadths of the diffraction lines. The microstrain calculated with TOPAS corresponds to an apparent maximum upper-limit strain given by $\varepsilon = \Delta d/d = \beta_D(2\theta)/4\tan(\theta)$, where β_D is the distortion related integral breadth [24]. The background refinement was made using a 10-term Chebyshev polynomial background function. Graphical images of the structure were designed with the VESTA software package [25]. The specific surface area of the as-synthesized powder was determined by measuring nitrogen physical adsorption isotherms at 77°C using a Gemini VII system (Micromeritics GmbH). Prior to the measurement, the sample was degassed at 120°C for 12 hours. The specific surface area was determined according to BET theory [26].

2.3. Electrochemical characterisation and structural characterisation during cycling

For the electrochemical characterization LiCaFeF₆ cathodes were cycled in two-electrode Swagelok cell against lithium metal counter electrodes. The cells were assembled inside a glovebox under Ar atmosphere. Glass fiber separators (GF/C, Whatman) and a solution of LiPF₆ (1 M) in ethylene carbonate (EC) and dimethyl carbonate (DMC) [1:1] as electrolyte (LP30, Merck) were used. *In situ* X-ray diffraction analysis was carried out using

1 of a dedicated laboratory diffraction setup equipped with a molybdenum micro focus rotating
2 anode generator ($\lambda = 0.71073 \text{ \AA}$) and a Pilatus 300K-W area detector. Details of this setup can
3
4 be found elsewhere [18]. A cathode containing 18.79 mg of LiCaFeF_6 active material was
5
6 cycled against the lithium metal anode at a current density of 6.095 mA g^{-1} corresponding to a
7
8 C-rate of $\sim C/20$. Two-dimensional diffraction images were recorded in transmission
9
10 geometry with an exposure time of 300 s. The intensities of two consecutive images were
11
12 added and integrated to one-dimensional diffraction patterns for further evaluation, resulting
13
14 in a time resolution of 10 min. For Rietveld refinement, the instrumental resolution function
15
16 was determined with an annealed CeO_2 sample and was described with a pseudo-Voigt profile
17
18 function of Thompson, Cox and Hastings [27]. A zero-point correction defined by Norby [28]
19
20 was used to correct for possible sample displacement errors of the active material and the Al
21
22 current collector. The background refinement was made using a 15-term Chebyshev
23
24 polynomial background function. The cycling was performed in optimized coin cell type
25
26 batteries [18] at galvanostatic conditions.
27
28
29
30
31
32

33
34 ^{57}Fe Mössbauer spectroscopic measurements were performed in transmission mode at
35
36 room temperature using a constant acceleration spectrometer with a $^{57}\text{Co}(\text{Rh})$ source. Isomer
37
38 shifts are given relative to that of $\alpha\text{-Fe}$ at room temperature. ^7Li magic-angle spinning (MAS)
39
40 nuclear magnetic resonance (NMR) spectroscopy was performed using a Bruker Avance 200
41
42 MHz spectrometer with 2.5 mm zirconia rotors. The magnetic field was $B_0 = 4.7 \text{ T}$
43
44 corresponding to a Larmor frequency of $\nu_L = 77.8 \text{ MHz}$. An aqueous 1 M LiCl solution was
45
46 used as a reference for the chemical shift of ^7Li (0 ppm). The values for the recycle delay and
47
48 the π/s pulse length were 1 s and $2.5 \mu\text{s}$, respectively. All NMR experiments were performed
49
50 at room temperature (298 K), with a spinning speed of 30 kHz, and a rotor synchronized
51
52 Hahn-echo sequence ($\pi/2\text{-}\tau\text{-}\pi\text{-}\tau\text{-}$ acquisition). XAS measurements were carried out at the
53
54 KMC-2 beamline of the BESSY II synchrotron light source in Berlin, Germany. Samples,
55
56 which were cycled to various states of charge, were mixed with graphite powder and pressed
57
58
59
60
61
62
63
64
65

1 into pellets. XAS spectra were recorded in the transmission mode at the Fe K-edge. Absolute
2 energy calibration of the monochromator was implemented by simultaneously measuring a
3 pure Fe reference foil. The intensities of the incident beam and the beams transmitted through
4 the sample and reference foil were recorded by use of three gas-filled ionization chambers. In
5 addition, the spectra of a FeF₂ and a FeF₃ reference were measured. The obtained data were
6 aligned and normalized, and the background was subtracted as described elsewhere [29] using
7 the ATHENA programme of the DEMETER software package[30].
8
9
10
11
12
13
14
15
16
17
18

19 3. Results and Discussion

20 3.1. Structural and morphological characterization

21
22 Fig. 1a shows the X-ray powder diffraction patterns and Rietveld refinement results of
23 LiCaFeF₆ after synthesis and after ball-milling with carbon and binder. The sharp Bragg
24 reflections of the as-synthesized material reveal good crystallinity, which is consistent with
25 the results from scanning electron microscopy (SEM) indicating a remarkable grain growth,
26 that yields particles with sizes of several micrometers (Fig. 1a, bottom). The crystal structure
27 can be assigned to the trigonal space group symmetry $P\bar{3}1c$ with $Z = 2$ (Fig. 1b). Rietveld
28 refinement yields lattice parameters of $a = 5.1298(1)$ Å and $c = 9.7765(2)$ Å (Table 1). The
29 refined atomic positions (Table 2) are in good agreement with colquiriite-type LiCaAlF₆ and
30 other isotype quaternary lithium metal fluoride compounds [19,31]. All cations are present in
31 a completely ordered arrangement. The refinement of the microstructure parameters yields an
32 apparent crystallite size of 240(+/-10) nm, which is significantly smaller than the visual
33 impression obtained from SEM images. This suggests that the particles in the micrographs
34 most likely consist of polycrystalline domains. The specific surface area determined by BET
35 amounts to $A_{BET} = 0.18$ m² g⁻¹. According to the relation $d_{BET} = 6/(\rho \cdot A_{BET})$, with the
36 theoretical density of LiCaFeF₆ of $\rho = 3.238$ g cm⁻³ [19], an average spherical grain diameter
37 of 10.3 µm can be estimated.
38
39
40
41
42
43
44
45
46
47
48
49
50
51
52
53
54
55
56
57
58
59
60
61
62
63
64
65

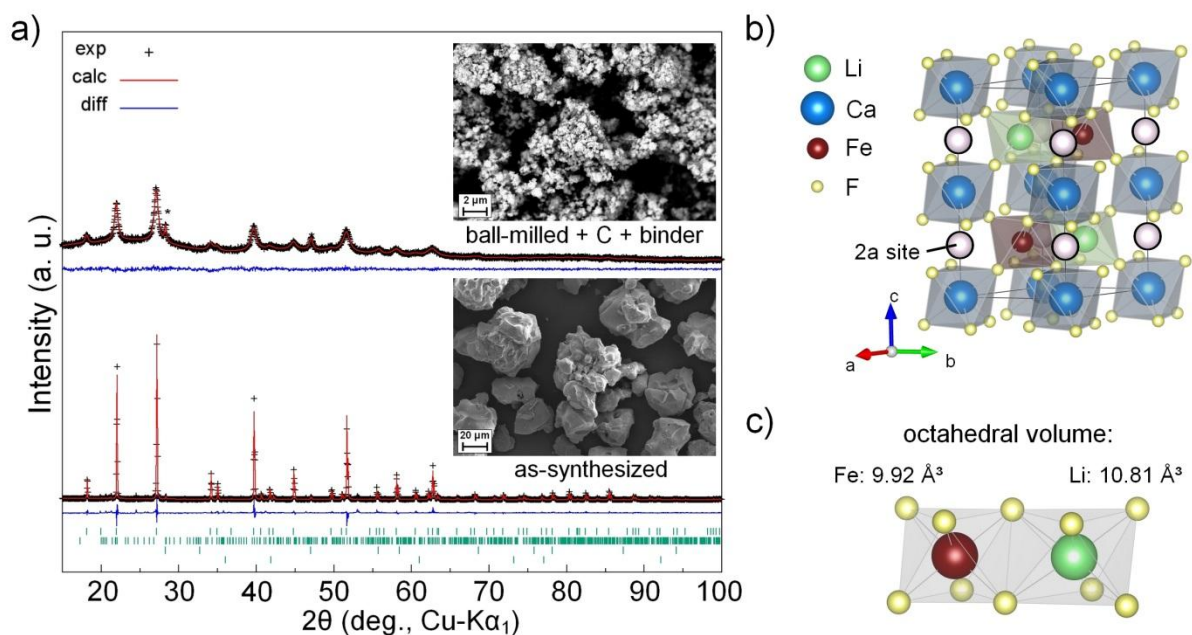


Fig. 1: a) Powder X-ray diffraction patterns and SEM micrographs of the as-synthesized LiCaFeF₆ (bottom) and after ball-milling with carbon and PVDF binder (top). Green ticks mark the positions of reflections of LiCaFeF₆ and impurity phases Li₃FeF₆, CaF₂, and LiF (from top to bottom). Asterisks mark CaF₂ impurity reflections in the ball-milled composite. b) Colquiriite-type crystal structure of LiCaFeF₆ with empty 2a site that is suggested for the insertion of additional lithium. c) The large ionic radius of initial Li⁺-ions, which are present in the pristine crystal structure, and the associated high [LiF₆]-octahedral volume stabilize the interlayer distance between [CaF]-layers.

This is significantly larger than the crystallite size obtained from XRD analysis and rather corresponds to the particles observed by SEM, indicating pronounced agglomeration and sintering of primary particles. The microstrain parameter determined by Rietveld analysis amounts to $\varepsilon = 1.38(2) \times 10^{-4}$. As minor impurity phases, small amounts of Li₃FeF₆ (~2.2 wt.-%), CaF₂ (~1.1 wt.-%) and LiF (< 1 wt.-%) were also detected. After applying ball-milling for 24 hours a LiCaFeF₆/C/binder nanocomposite was achieved and X-ray diffraction evidences that the colquiriite structure of LiCaFeF₆ can be maintained (Fig. 1a, top). However, the diffraction pattern of the electrode composite shows significant broadening of Bragg

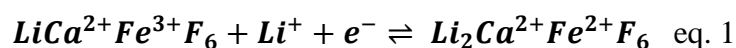
reflections. Rietveld refinement suggests that this is mainly due to a reduction in apparent crystallite size to approximately 26(4) nm. The crystallite size is in good accordance with the observations from SEM. Furthermore, an increase in microstrain to $\varepsilon = 3.1(1) \times 10^{-3}$ can be detected. The lattice constants of the ball-milled LiCaFeF_6 are $a = 5.1336(11) \text{ \AA}$ and $c = 9.7791(29) \text{ \AA}$. The cationic ordering within the unit cell is not affected by the high-energy ball-milling. This is a noteworthy difference as compared to other quaternary lithium metal fluorides with trirutile- and Na_2SiF_6 -type crystal structure, where ball-milling caused a significant decrease in the degree of cation order. An impact of ball-milling on fluorine atomic coordinates can be noticed by Rietveld refinement (Table 1) reflecting an increasing distortion of the hcp fluorine lattice.

Table 1: Lattice parameters and unit cell volume of LiCaFeF_6 directly after synthesis, after ball-milling and after cycling. Atomic coordinates from Rietveld refinement and isotropic thermal displacement parameters (B_{eq} of Li is taken from literature [31]) of LiCaFeF_6 after synthesis, after ball-milling and in the discharged state ($\text{Li}_{1.79}\text{CaFeF}_6$; determined by *ex situ* XRD).

Sample	a (Å)	c (Å)	Vol (Å ³)			
As-synthesized	5.1299(1)	9.7765(2)	222.80(1)			
Ball-milled	5.1336(11)	9.7791(29)	223.2(2)			
1 st discharge (2.0 V)	5.1414(7)	9.80128(210)	224.4(1)			
1 st charge (4.5 V)	5.1366(7)	9.78576(214)	223.6(1)			
2 nd discharge (2.0 V)	5.1408(7)	9.8030(21)	224.3(1)			
Atom	Wyckoff	x	y	z	occ	B_{eq}
Ca	2b	0	0	0	1	0.72(9)
Li	2c	1/3	2/3	1/4	1	1.00
Fe	2d	2/3	1/3	1/4	1	0.45(6)
F (as-synthesized)	12i	0.3649(9)	0.0137(7)	0.1378(3)	1	1.34(9)
F (ball-milled)	12i	0.3573(21)	0.0093(9)	0.1392(6)	1	1.34(9)
F (discharged)	12i	0.3622(15)	0.0137(7)	0.1328(6)	1	1.34(9)

3.2. Electrochemical characterisation

Electrochemical investigations were performed in a potential range from 2.0 to 4.5 V. Based on previous studies of lithium metal fluorides [15–18,21,32–35] it is assumed that the cations Ca^{2+} and Fe^{3+} are in the highest oxidation state within the applied operating voltage window. Lithium extraction from the host structure is therefore not expected. Hence cycling was started with discharging (insertion of Li^+ -ions) according to:



assuming $\text{Fe}^{3+}/\text{Fe}^{2+}$ to be the electrochemically active redox couple. Galvanostatic cycling ($I = 21.5 \mu\text{A} \triangleq C/20$) and cyclic voltammetry (Fig. 2a,c) were performed with cathodes containing 3.482 mg (3.079 mg cm^{-2}) and 3.561 mg (3.149 mg cm^{-2}) LiCaFeF_6 . The half-cells exhibit an open circuit voltage of 4.43 V vs. lithium. In the first cycle of the galvanostatic test, a discharge capacity of 112 mAh g^{-1} was achieved equivalent to ~ 0.91 Li per formula unit LiCaFeF_6 ($1 \text{ Li} \triangleq 123.59 \text{ mAh g}^{-1}$).

The discharge curve features a region with low slope corresponding to an increased capacity between 3.2 V and 2.6 V. Slow scan cyclic voltammetry reveals a maximum discharge current at 2.86 V, which is assigned to the reduction of Fe^{3+} to Fe^{2+} . Upon charging, the corresponding oxidation peak can be observed at 3.162 V. Accordingly, the cell potential curve features a low slope region between 2.8 V and 3.6 V during galvanostatic charging. During the following cycles, a slight increase in the electrode polarisation can be seen, as indicated by a shift of oxidation/reduction peaks in the cyclic voltammetry data. The cathode material shows good cyclic stability over 20 cycles (Fig. 2b). In the 20th cycle a discharge capacity of 94 mAh g^{-1} (0.76 eq. Li ; 76 % of its theoretical capacity) can still be achieved.

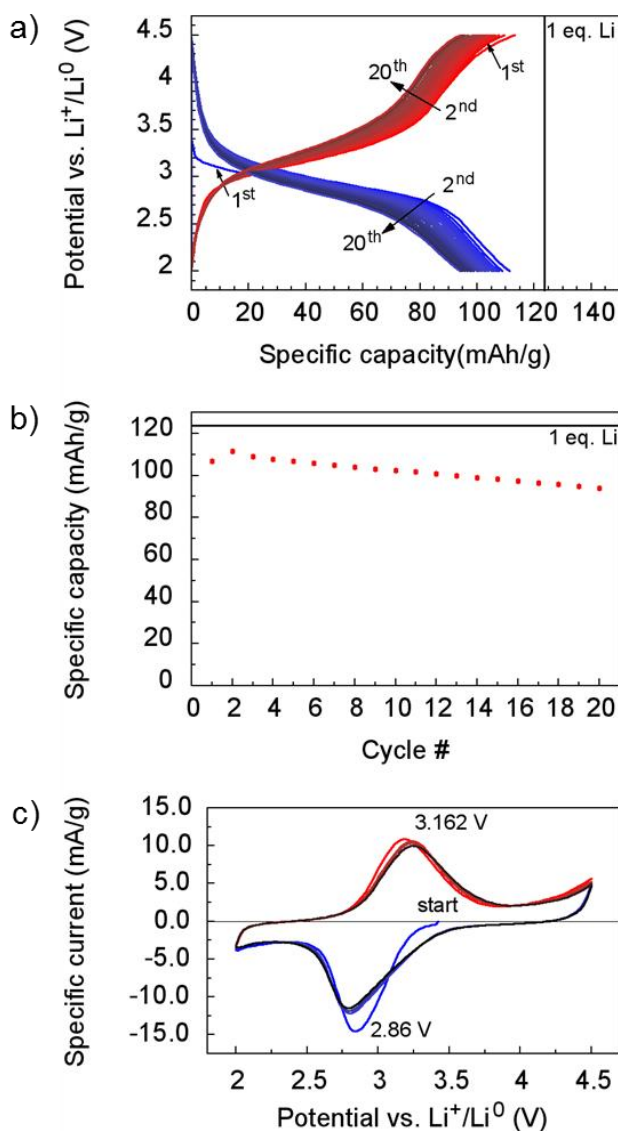


Fig. 2: a) Discharge (blue) and charge (red) profiles at galvanostatic cycling of LiCaFeF₆/C composite cathode at a rate of C/20. b) Discharge capacity of the LiCaFeF₆/C composite cathode during galvanostatic cycling at a rate of C/20. c) Slow-scan cyclic voltammetry (20 $\mu\text{V s}^{-1}$) of the LiCaFeF₆/C composite cathode within the potential range from 2.0 to 4.5 V.

3.3. ⁵⁷Fe Mössbauer spectroscopy

The ⁵⁷Fe Mössbauer spectra of LiCaFeF₆ in the as-synthesized state and after discharging to 2.0 V are displayed in Fig. 3. The spectrum of the as-synthesized sample predominantly consists of a narrow doublet with an isomer shift of $(0.44 \pm 0.01) \text{ mm s}^{-1}$ and a quadrupole splitting of $(0.55 \pm 0.25) \text{ mm s}^{-1}$. These parameters are characteristic of Fe³⁺.

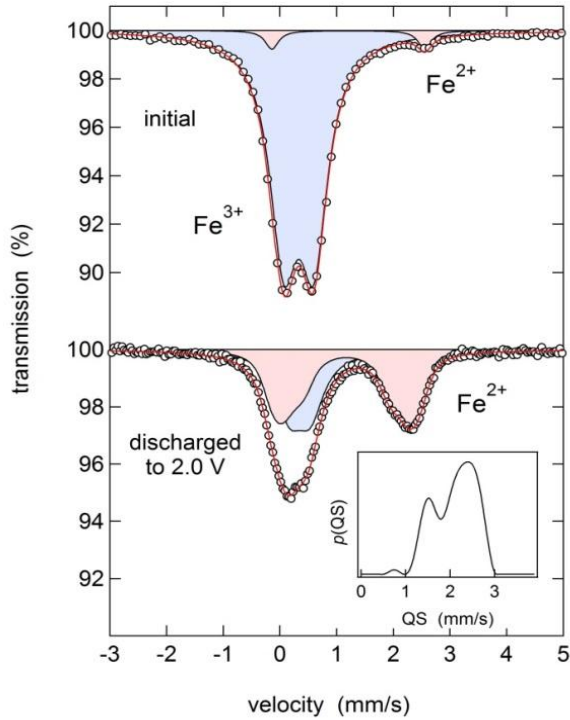


Fig. 3: ^{57}Fe Mössbauer spectra of LiCaFeF_6 in the as-prepared state and after discharging to 2.0 V. The experimental data points are given as white circles and the fits are given as red lines. Fe^{3+} and Fe^{2+} subspectra are given as blue and red doublets, respectively. The inset shows the distribution of quadrupole splittings used to describe the Fe^{2+} doublet after discharging to 2.0 V.

A second, much weaker doublet reveals an isomer shift of $(1.27 \pm 0.02) \text{ mm s}^{-1}$ and a quadrupole splitting of $(2.42 \pm 0.03) \text{ mm s}^{-1}$. Its area fraction amounts to 14.6 % and it has to be ascribed to the presence of a small amount of Fe^{2+} . After discharging to 2.0 V the Fe^{3+} contributions disappeared almost completely and the spectrum is dominated by a broad doublet consisting of two broad and highly asymmetric lines. The isomer shift of this doublet is $(1.21 \pm 0.01) \text{ mm s}^{-1}$ and it clearly shows that most of the Fe^{3+} has been converted to Fe^{2+} . The broad asymmetric lines can be described in terms of a distribution of quadrupole splittings. This distribution is ranging from 1 to 3 mm s^{-1} and it is remarkably similar to those obtained for LiNiFeF_6 [16] and LiMgFeF_6 [21] after lithium insertion.

3.4. ^7Li MAS NMR

Fig. 4 shows the ^7Li MAS NMR spectra of LiCaFeF_6 directly after synthesis, after milling with PVdF and carbon, and after discharging in a battery cell against Li metal down to 2.0 V. The spectrum of the sample obtained directly after synthesis shows two strong peaks at 367 ppm and 150 ppm. Such large NMR shifts are characteristic of paramagnetic neighbours in the direct environment of Li [36] and thus of the presence of Li-F-Fe bonds. This is confirmed by the fact that these two peaks show very broad patterns of spinning sidebands covering a range of ± 1500 ppm (not shown in the figure). Additionally, a small peak at 0 ppm is visible revealing the presence of Li in a diamagnetic environment, probably a small amount of LiF. After milling with carbon black and PVdF, the two peaks with the large shifts are still present but in a strongly broadened form. This hints at an increase of structural disorder induced by the milling and is consistent with similar observations on Li_2NiF_4 [34] and LiNiFeF_6 [18]. Since an alteration of cationic order could be excluded by XRD analysis, the broadening is most likely caused by a distortion of the fluorine lattice leading to variations in bond lengths and angles. After discharging to 2.0 V, the peaks at 367 ppm and 150 ppm disappeared completely and a new broad peak appeared at about 50 ppm. This is caused by intercalation of Li into the crystal structure of LiCaFeF_6 , which is accompanied by reduction of Fe^{3+} to Fe^{2+} (as evidenced by Mössbauer spectroscopy and XAS spectroscopy as discussed below). This changes the environment around Li and thus the interactions mediated via the Li-F-Fe bonds. The much smaller shifts caused by the presence of the Fe^{2+} neighbors in comparison to the Fe^{3+} environments is consistent with earlier experiments on $\text{Li}_2\text{Fe}_{1-y}\text{Mn}_y\text{SiO}_4$ [37], $\text{LiMn}_{0.6}\text{Fe}_{0.4}\text{PO}_4$ [38], and LiNiFeF_6 [18]. The increased intensity of the peak at 0 ppm may be caused by residues of the Li salt from the electrolyte.

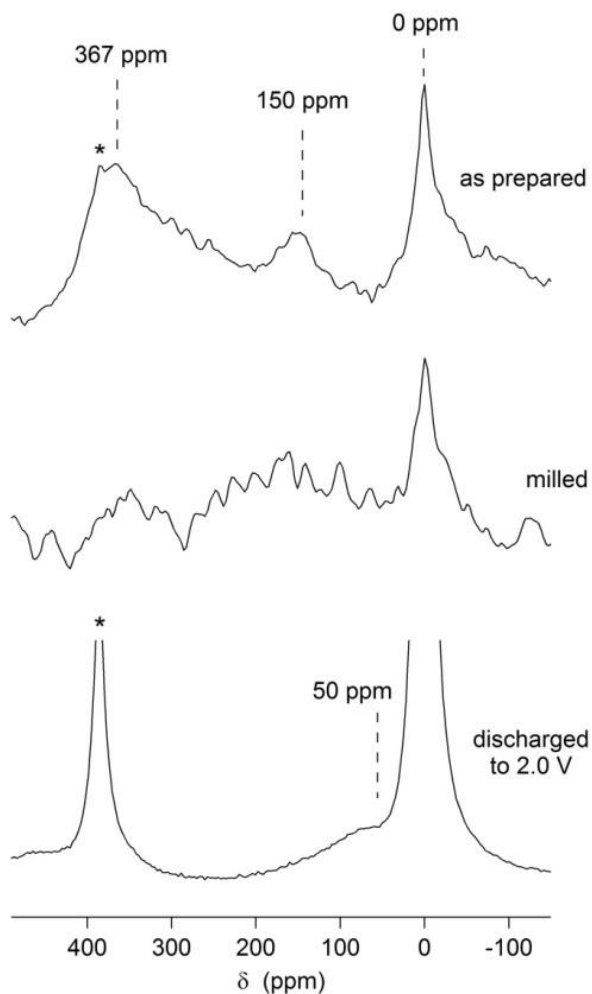


Fig. 4: ^7Li MAS NMR spectra of LiCaFeF_6 directly after synthesis, after milling with PVdF and carbon, and after discharging against Li metal down to 2.0 V. Spinning sidebands are marked with an asterisk.

3.5. XANES spectroscopy

The normalised X-ray absorption near edge structure (XANES) spectra of LiCaFeF_6 measured at the Fe-K-edge of various samples cycled to different states of charge and discharge and of the reference materials are shown in Fig. 5. All spectra feature a pre-edge region which corresponds to the $1s \rightarrow 3d$ electric-dipole-forbidden, but quadrupole-allowed transition [39]. Its presence gives hint on a distortion of $[\text{FeF}_6]$ octahedra.

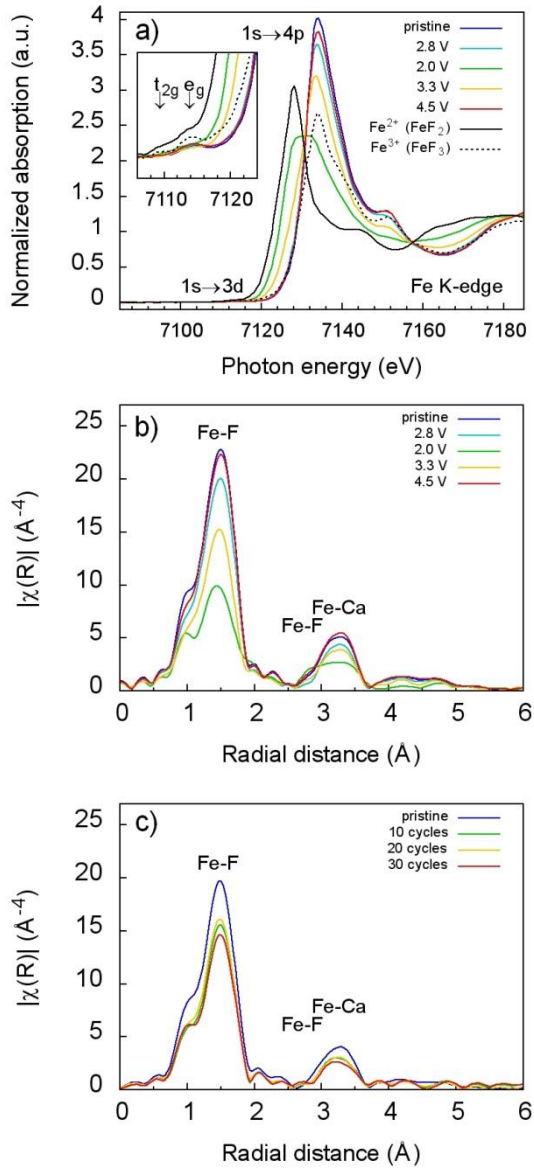


Fig. 5: Normalised X-ray absorption spectra (a) and Fourier transforms of the k^3 -weighted EXAFS signals $X(k)$ (b) at the Fe K-edge of $\text{Li}_{1+x}\text{CaFeF}_6$ measured in the pristine state ($\text{Li}_{1.00}\text{CaFeF}_6$) and *ex situ* after cycling to various electrochemical states of discharge (2.8 V ($\text{Li}_{1.42}\text{CaFeF}_6$), 2.0 V ($\text{Li}_{1.77}\text{CaFeF}_6$)) and charge (3.3 V ($\text{Li}_{1.42}\text{CaFeF}_6$), 4.5 V ($\text{Li}_{1.00}\text{CaFeF}_6$)). Further spectra are measured in the charged state at 4.5 V after cycling over a period of 10, 20, and 30 cycles (c). Labels of peaks in the Fourier transforms assign the coordination shell. The inset in (a) shows an expanded view of the pre-edge region.

1 The maximum of the vertically rising main edge can be assigned to the $1s \rightarrow 4p$
2 transition [39]. In the pristine material the position of the $1s \rightarrow 4p$ peak is very similar to that
3 of the Fe^{3+} -containing reference. Upon discharge a chemical shift of the main absorption edge
4 to lower energies can be detected. After discharge to 2.8 V ($x = 0.42$ in $\text{Li}_{1+x}\text{CaFeF}_6$; the Li
5 content was calculated based on the measured capacity) a minor shift has occurred, though the
6 edge is still located in close proximity to the Fe^{3+} reference. The Fe K-edge of the sample
7 discharged to 2.0 V ($x = 0.77$) is also located between the edges of the two reference spectra,
8 however, it is now closer to the edge of the Fe^{2+} -containing reference. With regard to the
9 amount of inserted lithium of $x = 0.77$ a mismatch between the edge of the discharged sample
10 and the edge of the Fe^{2+} reference is expected and serves as indication of a mixed-valent state
11 of iron. As the material is charged to 3.3 V ($x = 0.42$) a reverse shift of the Fe K-edge to
12 higher energies can be noticed. In the completely charged state at 4.5 V the original position
13 of the Fe K-edge of the Fe^{3+} reference is achieved demonstrating the reversibility of the
14 electrochemical reaction. These observations evidence the active $\text{Fe}^{3+}/\text{Fe}^{2+}$ redox couple and
15 are in accordance with the results from Fe-Mössbauer spectroscopy. Moreover, the presence
16 of the $1s \rightarrow 3d$ transition in the pre-edge region and its splitting into a doublet of the t_{2g} and e_g
17 orbital hints on an asymmetric distortion of the Fe-F bonds [39–43].
18
19
20
21
22
23
24
25
26
27
28
29
30
31
32
33
34
35
36
37
38
39
40
41
42

43 **3.6. Structural characterization upon cycling**

44 **3.6.1. *In situ* X-ray diffraction**

45
46
47
48
49
50
51
52
53
54
55
56
57
58
59
60
61
62
63
64
65
Cycling of the $\text{LiCaFeF}_6/\text{Li}$ cell was performed between 2.0 V and 4.5 V under
constant current conditions with a rate of C/20 over three half cycles. At the end of each
discharge and charge cycle, the cell was held at the constant cut-off voltage for two hours to
allow for the relaxation of kinetic effects and to obtain a defined state of charge.

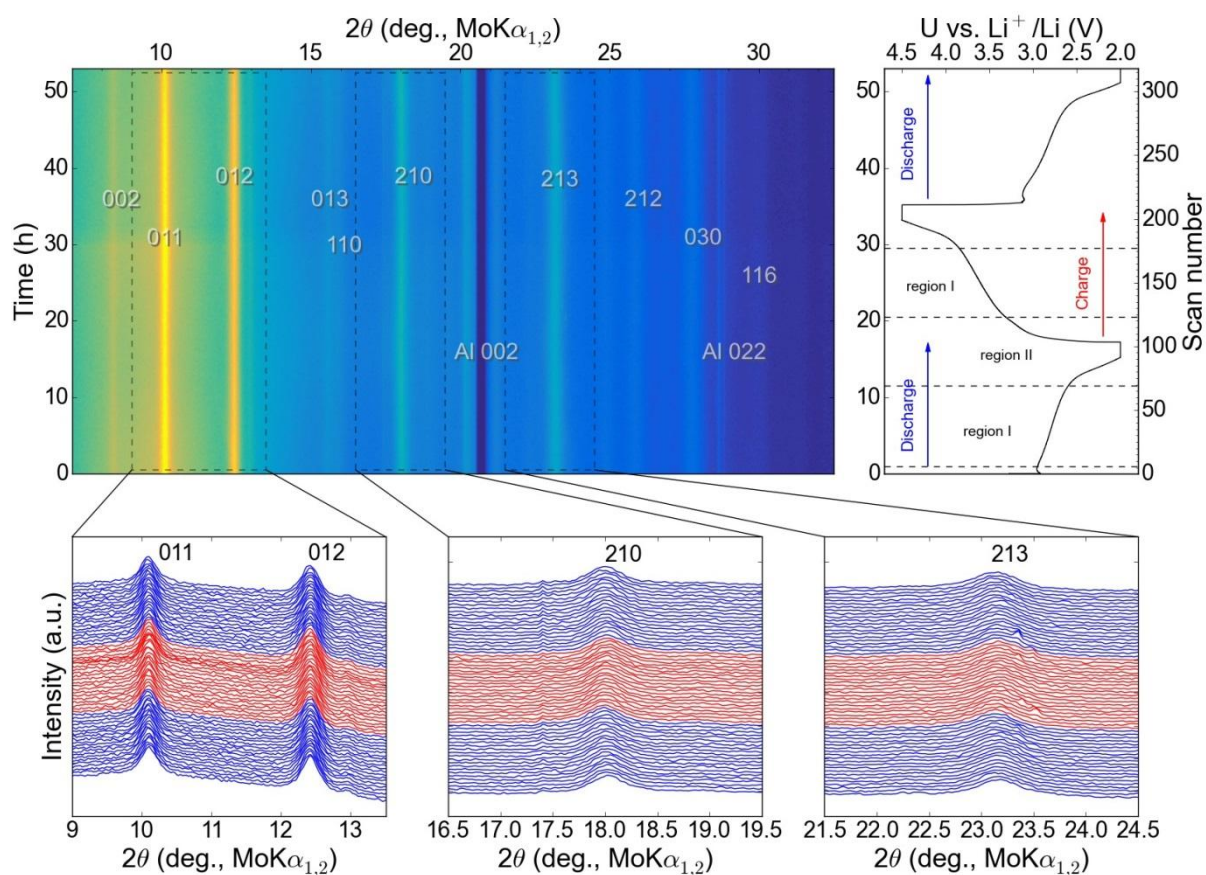


Fig. 6: Evolution of *in situ* X-ray diffraction patterns of LiCaFeF_6 during the first three half-cycles.

Fig. 6 shows a contour plot of the diffracted intensities during the *in situ* XRD experiment in the 2θ region between 7° and 32.5° , together with the electrochemical data and enlarged views of the diffraction patterns in selected 2θ regions. The recorded cell voltage shows regions with reduced slope, corresponding to regions of increased capacity (region I) and regions with higher slope (region II). Region I is found between 2.9 V and 2.6 V in discharge and between 3.3 V and 3.8 V during charge. In the first cycle a discharge capacity of 98.7 mAh g^{-1} was obtained, which corresponds to $x = 0.80$ Li per formula unit $\text{Li}_{1+x}\text{CaFeF}_6$. The charge capacity in the first cycle is 104.8 mAh g^{-1} and is thus higher than the discharge capacity, which suggests that all of the inserted lithium is completely extracted during charging. An extraction of further lithium from the host structure is unlikely and was

1 not observed by *in situ* XRD for the quaternary lithium metal fluoride LiNiFeF_6 either. During
2 the whole experiment, the positions as well as the intensities of Bragg reflections of LiCaFeF_6
3 stay nearly the same. This shows that the colquiriite structure is stable during lithiation and
4 delithiation. It should be noted that the reflections do not show any significant line broadening
5 and no additional reflections occur, which would indicate the formation of additional phases
6 confirming that Li insertion/extraction occurs through solid solution. Only a careful
7 examination reveals that the reflections slightly shift towards lower 2θ -angles during
8 discharge and shift back to their initial positions during subsequent charge. The data of the
9 second discharge cycle confirm the reversibility of these very weak structural changes.
10
11
12
13
14
15
16
17
18
19
20
21

22 Fig. 7 shows the results of lattice parameters and strain parameters determined by the
23 Rietveld refinement. Selected diffraction patterns taken at different states of the reduction
24 process upon first discharge, together with the calculated patterns are displayed in
25 Supplementary Fig. S1. The refinement results confirm that in the whole concentration range
26 of the experiment of up to a maximum of $x = 0.8$ Li, the compound $\text{Li}_{1+x}\text{CaFeF}_6$ exists as a
27 single phase solid solution system. All diffraction patterns can be described by a single
28 structural model based on the colquiriite structure (occupation of Wyckoff positions according
29 to Tab. 2). The course of calculated lattice parameters (Fig. 7) exhibits only a minor variation
30 of unit cell dimensions upon cycling. At the beginning the lattice parameters are $a =$
31 $5.1344(6)$ Å and $c = 9.7892(20)$ Å. The initial unit cell volume hence amounts to $V = 223.2(1)$
32 Å³. During discharge the cell potential rapidly flattens into the plateau-like region (region I).
33 In the discharge interval up to an inserted amount of $x = 0.55$ Li, a volume increase of only
34 approximately 0.2 % to $V = 223.86(8)$ Å³ occurs. This expansion is attributed to the very
35 small increase in both lattice parameters a and c . The a lattice parameter increases by 0.06 %
36 to $a = 5.1377(7)$ Å. The c lattice parameter increases by 0.04 % to $c = 9.7926(23)$ Å. Further
37 discharge leads to a steeper course of the cell potential (region II). An amount of $x = 0.75$ Li
38 is transferred into the host structure until the cut-off voltage of 2.0 V is reached.
39
40
41
42
43
44
45
46
47
48
49
50
51
52
53
54
55
56
57
58
59
60
61
62
63
64
65

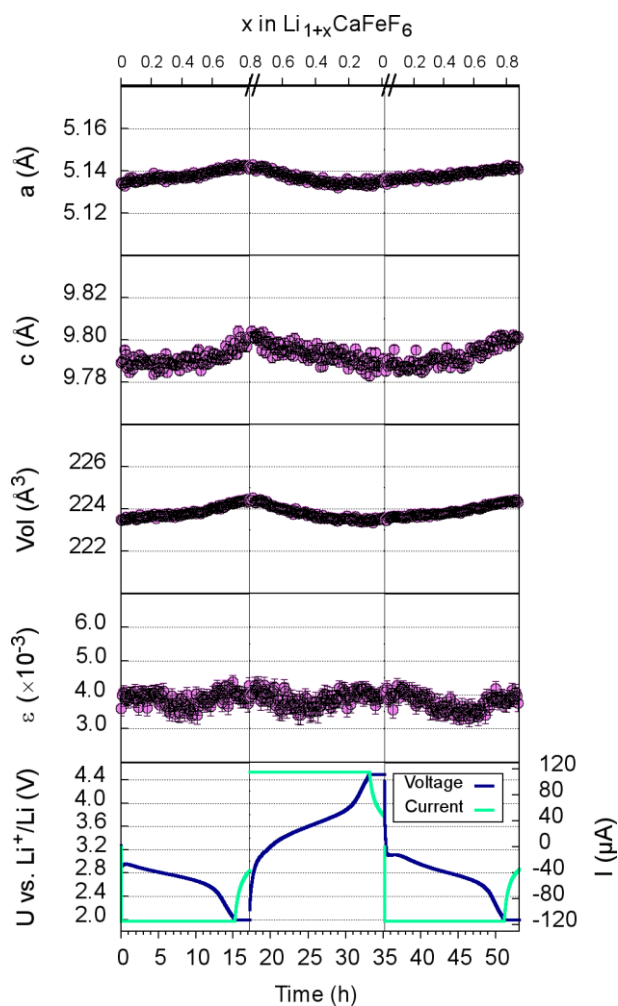


Fig. 7: Rietveld refinement results of lattice metric and microstrain of LiCaFeF_6 as a function of Li content electrochemical state.

In this interval, both lattice parameters increase more rapidly but still to limited extent up to $a = 5.1430(7) \text{ \AA}$ and $c = 9.7930(23) \text{ \AA}$. During the constant voltage step at 2.0 V the lattice constants level off at values of $a = 5.1415(7) \text{ \AA}$ and $c = 9.8013(22) \text{ \AA}$. Compared to the uncycled state this corresponds to an increase by 0.14 % and 0.12 %. At the end of discharge ($x = 0.8 \text{ Li}$) the volume is $V = 224.38(8) \text{ \AA}^3$. Thus, the maximum volume expansion amounts to less than 0.5 % over the whole range of discharge. Despite this remarkably small expansion of the host structure of LiCaFeF_6 , the Li-insertion is accompanied by a slight increase in microstrain. The course of the refined strain parameter ϵ exhibits an increase from initially $3.6(2) \times 10^{-3}$ to $4.2(2) \times 10^{-3}$.

1 The following charge cycle and the subsequent, second discharge cycle confirm the
2 reversibility of the structural processes. Upon extraction of the previously inserted Li^+ -ions
3
4 the lattice parameters decrease again in a symmetrical course and finally achieve $a =$
5
6 $5.1365(7) \text{ \AA}$ and $c = 9.7857(22) \text{ \AA}$ at the end of charge, which almost coincides with the
7
8 initial values. This corresponds to a volume expansion of only approximately 0.05 % as
9
10 compared to the uncycled state.
11
12
13

14 **3.6.2. *Ex situ* X-ray diffraction**

15
16
17 *In situ* XRD has proven exceptionally high structural stability of LiCaFeF_6 against Li-
18
19 insertion. For a more detailed investigation of even minimal changes an *ex situ* sample, that
20
21 was cycled to the discharged state at 2.0 V ($x = 0.79$), was analysed by XRD and Rietveld
22
23 refinement. A presentation of the measured diffraction data and the calculated pattern from
24
25 Rietveld analysis is shown in Supplementary Fig. S1. The calculated lattice parameters of
26
27 $\text{Li}_{1.79}\text{CaFeF}_6$ are $a = 5.1498(5) \text{ \AA}$ and $c = 9.8110(16) \text{ \AA}$. The values are in good agreement
28
29 with values obtained by *in situ* XRD. Besides the minor lattice parameter expansion, a slight
30
31 deviation of F-anions from their original atomic positions can be detected indicating a slight
32
33 distortion of the fluorine lattice (Table1). Presumably, such distortion is the consequence of
34
35 incorporation of additional lithium into the crystal structure and, moreover, is caused by the
36
37 partial reduction of Fe^{3+} to Fe^{2+} . The atomic coordinates of the cations remain unchanged,
38
39 since these occupy special sites in the colquiriite structure and do not have any positional
40
41 degree of freedom.
42
43
44
45
46
47
48
49

50
51 Due to the low X-ray scattering power of lithium it is hard to determine the precise
52
53 distribution of inserted Li^+ -ions. Nevertheless, placing Li atoms onto different sites in the
54
55 Rietveld refinement may help to infer the positions of Li in the crystal structure.
56
57 Theoretically, the crystal structure of LiCaFeF_6 offers three different octahedrally coordinated
58
59 empty sites, namely the 2a, 4e and 6g site. A slight, gradual change in intensities of distinct
60
61
62
63
64
65

1 Bragg reflections (020 and 114 reflection) hints on a change in Li concentration (see
2 Supplementary Fig. S2). When possible lithium occupation of the 4e or 6g site is taken into
3
4 account, the refinement shows lower quality. However, if an occupation of the 2a site is
5
6 assumed, a noticeable improvement of the R_{wp} value can be achieved (see Supplementary Fig.
7
8 S3). A refinement of the site occupancy parameter yields $occ_{Li2} = 0.72(6)$, which is in
9
10 satisfying accordance with the amount of inserted Li that was calculated by the charge
11
12 transferred during the discharge ($x = 0.79$). A corresponding expansion of the surrounding
13
14 fluorine octahedron from approximately 12.30 \AA^3 to 13.34 \AA^3 corroborates the assumption of
15
16
17 Li insertion on the 2a site.
18
19
20
21
22
23

24 **3.6.3. EXAFS spectroscopy**

25
26 The Fourier transforms of the k^3 -weighted EXAFS signals $X(k)$ at the Fe K-edge of the
27
28 LiCaFeF₆ cathode material in the pristine state as well as at differently charged and
29
30 discharged states are depicted in Fig. 5b. In the Fourier transform the first peak is located at
31
32 approximately 1.5 \AA , which is assigned to the bond between iron and fluorine atoms in the 1st
33
34 shell around Fe absorbers. The signal at approximately 3.3 \AA in the Fourier transform can be
35
36 assigned to the higher-order Fe-Ca distance. On the left side of this signal a further peak at
37
38 approximately 2.9 \AA is present corresponding to the higher order Fe-F distance. For the
39
40 material that was discharged to 2.8 V and 2.0 V a progressive reduction in amplitude of the
41
42 signals, in particular of the first Fe-F signal, can be observed. This is assigned to a change in
43
44 the length of the first shell Fe-F bond and is in agreement with the results from XRD. It is
45
46 assumed that these changes originate from the reduction of Fe³⁺ to Fe²⁺ upon discharge as it
47
48 has been proven by XANES and Mössbauer spectroscopy. In addition, the signal exhibits
49
50 broadening, which might be caused by local variations in bond lengths and possibly is
51
52 affected by differences in Li concentration in the host structure.
53
54
55
56
57
58
59
60
61
62
63
64
65

1 After charging the material to 3.3 V an increase in the amplitude can be seen and in
2 the fully charged state at 4.5 V the amplitude nearly achieves its initial level. The signals in
3
4 the Fourier transform of the sample at 4.5 V are in good agreement with the signals of the
5
6 uncycled sample, demonstrating the good reversibility of local structural changes.
7
8

9 Further EXAFS spectra were recorded at the Fe K-edge of samples in the charged state
10
11 at 4.5 V after cycling over a period of 10, 20, and 30 cycles (Fig. 5c). In comparison to the
12
13 uncycled state a slight reduction in the amplitudes of the Fourier transforms can be observed
14
15 at higher cycle numbers. Nevertheless, after cycling over a long period of 30 cycles the signal
16
17 still remains quite stable and no significant aging phenomena, such as formation of a new
18
19 phase or alteration in the local structure of the original material, are observed, indicating a
20
21 considerable stability of the electrode host structure.
22
23
24
25
26
27

28 **4. The zero-strain lithium insertion mechanism**

29
30

31 The results from structural analysis consistently demonstrate that the colquiriite host
32
33 structure of $\text{Li}_{1+x}\text{CaFeF}_6$ cathode material is retained at any state of charge in the voltage
34
35 window between 2.0 and 4.5 V. The material can be cycled as a pure solid solution system in
36
37 the lithium concentration range of $0 \leq x \leq 0.8$. Tab. 3 summarizes the calculated lattice
38
39 parameters, bond lengths and polyhedral volumes of the cathode material at the uncycled state
40
41 and in the discharged state at 2.0 V. Based on the results from *ex situ* X-ray diffraction it is
42
43 assumed that inserted Li^+ -ions occupy the previously empty crystallographic 2a site (Fig. 1b).
44
45 After the insertion of additional lithium expansion of the *a* lattice parameter and the *c* lattice
46
47 parameter by 0.14 % and 0.13 %, respectively, can be detected by *in situ* XRD. Hence, the
48
49 overall volume expansion amounts to < 0.5 %, which is exceptionally low compared to the
50
51 volume changes observed for other cathode materials. Also the *c/a* ratio only changes by 0.01
52
53 % upon discharge. This small and approximately isotropic change in lattice parameters is
54
55 reflected by a likewise small increase of the microstrain parameter ε (Fig. 7). In order to
56
57
58
59
60
61
62
63
64
65

1 obtain a better understanding of the exceptionally high stability of the host structure, the
2 distribution of cations in the structure, as well as the linkage between their corresponding
3
4 fluorine octahedra need to be considered in more detail. The structure consists of a packing of
5
6 two types of alternating slabs, one made of [CaF₆]-octahedra (Wyckoff position 2b) and the
7
8 other made of [FeF₆]- and [LiF₆]-octahedra. Each [CaF₆]-octahedron is connected via corners
9
10 with three [FeF₆]-octahedra (Wyckoff positions 2c) and three [LiF₆]-octahedra (Wyckoff
11
12 positions 2d) from layers below and above. Edge-sharing with these octahedra is rather
13
14 unlikely due to the very large volume of [CaF₆]-octahedra (15.46 Å³). However, [FeF₆]- and
15
16 [LiF₆]-octahedra are edge-connected, though they also differ in volume. The volume of
17
18 [LiF₆]-octahedra amounts to 10.81 Å³, whereas [FeF₆]-octahedra are noticeably smaller with a
19
20 volume of 9.92 Å³. As a result, the larger [LiF₆]-octahedron functions as a crucial spacer
21
22 keeping the adjacent [CaF₆]-slabs distant in *c*-direction. This can compensate volume changes
23
24 caused by the increase of iron ionic radius when Fe³⁺ is reduced to Fe²⁺ upon Li insertion. As
25
26 Rietveld analysis of the discharged sample shows, the octahedral volume of Fe-octahedra
27
28 amounts to 10.29 Å³ after the insertion of 0.79 Li per Li_{1+x}CaFeF₆. Nevertheless, the [LiF₆]-
29
30 octahedra still have a larger volume (11.69 Å³) and hence Fe-F bond lengths do not decisively
31
32 influence the dimensions of the unit cell.
33
34
35
36
37
38
39
40

41 In their extensive comparative study Pawlak et al. [46] systematically investigated the
42
43 structural parameters of various LiMe^{II}Me^{III}F₆ compounds with colquiriite-type crystal
44
45 structure. It was shown that ion radii of the Me^{II}- and the Me^{III}-ion differently affect the lattice
46
47 parameters. Substitution of the divalent Me^{II}-cation on the 2b site, as for instance Ca^{II} by the
48
49 larger Sr^{II}, does strongly affect the *c*-lattice parameter while the trivalent Me^{III}-ion on the 2c
50
51 site does not have significant impact on the *c*-axis. Even though there is a correlation between
52
53 the size of the Me^{III}-ion and the *a*-lattice parameter, the effect is substantially smaller allowing
54
55 the interatomic Me^{III}-F distances to vary by up to 0.1 Å without influencing the *a*-axis.
56
57
58
59
60
61
62
63
64
65

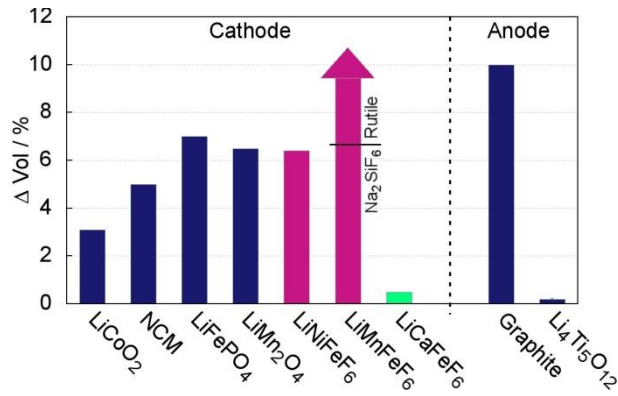


Fig. 8: Comparison of the relative volume change of LiCaFeF₆ cathode material with that of other quaternary LiMe^{II}FeF₆ compounds [17,18] as well as with that of commercially used electrode materials [1,4,11,44,45].

Hence, the octahedra that are coordinating the electrochemically active Fe^{III}-ions are affecting the lattice parameters of LiCaFeF₆ the least. According to Viebahn [19] the structure type of quaternary LiMe^{II}Me^{III}F₆ compounds depends on the ratio of ionic radii $r_{Me^{II}}/r_{Me^{III}}$. Therefore, a possible transformation from the colquiriite structure into Na₂SiF₆-type structure upon the reduction of Fe³⁺ to Fe²⁺ should be taken into consideration. Galy and Andersson showed that such transformation is based on a simple geometric relation throughout which the hcp fluorine lattice is retained and only the way of octahedra linkage is changed [47]. Based on the example of the solid solution series LiCd_{1-x}Mn_xCrF₆, Viebahn [19] determined a critical limit of $r_{Me^{II}}/r_{Me^{III}} = 1.48$ below which the colquiriite structure is transformed into Na₂SiF₆-type structure. Assuming a maximum of inserted lithium of $x = 1$ in Li_{1+x}CaFeF₆ and a complete reduction of iron to Fe²⁺, the ratio of ionic radii should be approximately 1.47, and is thus slightly below the critical lower phase boundary of the colquiriite structure. However, Viebahn [19] also showed that the Na₂SiF₆ structure can only be formed if the ionic radii do not differ by more than 15 %. Due to the large size of Ca²⁺, this is not the case for LiCaFeF₆ [48]. Hence, the stability of the colquiriite host structure of LiCaFeF₆ can be ensured at any valence state of Fe between 2+ and 3+. Regarding the electrochemical voltage profile, the

1
2
3
4
5
6
7
8
9
10
11
12
13
14
15
16
17
18
19
20
21
22
23
24
25
26
27
28
29
30
31
32
33
34
35
36
37
38
39
40
41
42
43
44
45
46
47
48
49
50
51
52
53
54
55
56
57
58
59
60
61
62
63
64
65

LiCaFeF₆ cathode material shows very similar features to other quaternary lithium metal fluorides LiMe^{II}FeF₆ [16–18,20,21]. This is attributed to the typical shape of the charge and discharge profile of the electrochemically active Fe³⁺/Fe²⁺ redox couple that all compounds have in common as Mössbauer spectroscopy [16,17,21] and X-ray absorption spectroscopy [18] reveal. However, its highly stable colquiriite structure distinguishes LiCaFeF₆ from other fluorides. The structural stability is reflected in a better cycling stability as compared to that of quaternary fluorides with trirutile [16,20,21] or Na₂SiF₆-type [17] structure demonstrating the clear benefits of the colquiriite structure. Fig. 8 shows a comparison of the relative volume change of LiCaFeF₆ with volume changes taking place in other quaternary lithium metal fluorides and different commercial electrode materials. The illustration shows that comparably small volume change is only provided by the zero-strain anode material Li₄Ti₅O₁₂ (LTO) [11]. Fig. 8 also reflects the fact that there is no commercial cathode material with strains that are similar to those reported here. Another positive electrode material showing a similar zero-strain effect is Li_{1+x}Rh₂O₄ [13,14] which, however, it is not used in applications. In contrast to LiCaFeF₆, both zero-strain materials Li₄Ti₅O₁₂ and Li_{1+x}Rh₂O₄ exhibit a two-phase transformation upon lithium insertion. Despite the minor lattice parameter changes, the formation of coherent phase boundaries taking place during a two-phase transformation may lead to very small lattice strain between crystal domains of different Li content. Such structural instabilities may still accumulate and lead to mechanical damage during cycling. This can be avoided by a pure solid-solution system like Li_{1+x}CaFeF₆. LiCaFeF₆ is made from abundant elements and potentially is a cheap and reliable material and therefore very promising for future application in safe and reliable lithium ion batteries.

5. Conclusion

The quaternary lithium fluoride LiCaFeF₆ with colquiriite crystal structure was synthesized by a solid-state reaction and processed to a conductive electrode composite via

1 high-energy ball-milling. The as-synthesized LiCaFeF_6 as well as the ball-milled
2 $\text{LiCaFeF}_6/\text{C}/\text{binder}$ composite were characterised structurally and morphologically showing
3
4 that the colquiriite structure is preserved upon milling. Electrochemical cycling was
5 performed against a lithium anode in the potential range from 2.0 V to 4.5 V. In the first cycle
6
7 of the galvanostatic test, a discharge capacity of 112 mAh g^{-1} can be achieved. Slow scan
8
9 cyclic voltammetry reveals a maximum discharge current at 2.86 V, which is assigned to the
10
11 reduction of Fe^{3+} to Fe^{2+} . The electrochemically active redox couple $\text{Fe}^{3+}/\text{Fe}^{2+}$ was confirmed
12
13 by Mössbauer spectroscopy and X-ray absorption spectroscopy.
14
15
16
17
18

19 In comparison to other quaternary lithium metal fluorides the compound LiCaFeF_6
20
21 with colquiriite-type crystal structure shows by far the most promising results regarding its
22
23 properties as cathode material for use in lithium ion batteries. The structural properties of
24
25 LiCaFeF_6 upon cycling in a lithium-ion battery were analysed by means of *in situ* and *ex situ*
26
27 XRD as well as X-ray absorption spectroscopy (EXAFS). The results show that due to an
28
29 appropriate arrangement of polyhedra and interatomic distances, a very flexible and reversible
30
31 response to Li uptake is guaranteed yielding minimum changes in lattice parameters and a
32
33 total change in unit cell volume of < 0.5 % for an uptake of 0.8 mole Li per formula unit. The
34
35 reversibility and long-term stability was furthermore confirmed. In Lithium-ion batteries such
36
37 “zero-strain“ behaviour is only observed for the $\text{Li}_4\text{Ti}_5\text{O}_{12}$ (LTO) anode material and up to
38
39 now no other commercially used cathode material for Li-ion batteries with comparable
40
41 properties is known, which makes LiCaFeF_6 a promising candidate for future energy storage
42
43 applications.
44
45
46
47
48
49
50
51
52

53 **Acknowledgement**

54 The author wishes to thank the HZB for allocated beam time and their technical support.
55
56
57
58
59
60
61
62
63
64
65

References

- 1
2
3 [1] X.Q. Yang, X. Sun, S.J. Lee, J. McBreen, S. Mukerjee, M.L. Daroux, X.K. Xing, In Situ
4
5 Synchrotron X-Ray Diffraction Studies of the Phase Transitions in $\text{Li}_x \text{Mn}_2 \text{O}_4$
6
7 Cathode Materials, *Electrochem. Solid-State Lett.* 2 (1999) 157–160.
8
9
- 10 [2] J. Christensen, J. Newman, A Mathematical Model of Stress Generation and Fracture in
11
12 Lithium Manganese Oxide, *J. Electrochem. Soc.* 153 (2006) A1019.
13
14 doi:10.1149/1.2185287.
15
16
- 17 [3] D. Wang, X. Wu, Z. Wang, L. Chen, Cracking causing cyclic instability of LiFePO_4
18
19 cathode material, *J. Power Sources.* 140 (2005) 125–128.
20
21 doi:10.1016/j.jpowsour.2004.06.059.
22
23
- 24 [4] A.K. Padhi, Phospho-olivines as Positive-Electrode Materials for Rechargeable Lithium
25
26 Batteries, *J. Electrochem. Soc.* 144 (1997) 1188. doi:10.1149/1.1837571.
27
28
- 29 [5] P. Arora, Capacity Fade Mechanisms and Side Reactions in Lithium-Ion Batteries, *J.*
30
31 *Electrochem. Soc.* 145 (1998) 3647. doi:10.1149/1.1838857.
32
33
- 34 [6] O. Dolotko, A. Senyshyn, M.J. Muhlbauer, K. Nikolowski, F. Scheiba, H. Ehrenberg,
35
36 Fatigue Process in Li-Ion Cells: An In Situ Combined Neutron Diffraction and
37
38 Electrochemical Study, *J. Electrochem. Soc.* 159 (2012) A2082–A2088.
39
40 doi:10.1149/2.080212jes.
41
42
- 43 [7] W.H. Woodford, Y.-M. Chiang, W.C. Carter, Electrochemical shock in ion-intercalation
44
45 materials with limited solid-solubility, *J. Electrochem. Soc.* 160 (2013) A1286–A1292.
46
47
- 48 [8] J. Cho, Y.J. Kim, B. Park, Novel LiCoO_2 Cathode Material with $\text{Al}_2 \text{O}_3$ Coating for a
49
50 Li Ion Cell, *Chem. Mater.* 12 (2000) 3788–3791. doi:10.1021/cm000511k.
51
52
- 53 [9] J. Cho, Y.J. Kim, T.-J. Kim, B. Park, Zero-Strain Intercalation Cathode for Rechargeable
54
55 Li-Ion Cell, *Angew. Chem. Int. Ed.* 40 (2001) 3367–3369.
56
57
- 58 [10] Z. Chen, J.R. Dahn, Studies of LiCoO_2 Coated with Metal Oxides, *Electrochem.*
59
60 *Solid-State Lett.* 6 (2003) A221. doi:10.1149/1.1611731.
61
62
63
64
65

- 1
2
3
4
5
6
7
8
9
10
11
12
13
14
15
16
17
18
19
20
21
22
23
24
25
26
27
28
29
30
31
32
33
34
35
36
37
38
39
40
41
42
43
44
45
46
47
48
49
50
51
52
53
54
55
56
57
58
59
60
61
62
63
64
65
- [11] T. Ohzuku, A. Ueda, N. Yamamoto, Zero-Strain Insertion Material of $\text{Li}[\text{Li}/3\text{Tis}/3]\text{O}_4$ for Rechargeable Lithium Cells, *J. Electrochem. Soc.* 142 (1995) 1431–1435.
- [12] S. Scharner, W. Weppner, P. Schmid-Beurmann, Evidence of Two-Phase Formation upon Lithium Insertion into the $\text{Li}_{1.33}\text{Ti}_{1.67}\text{O}_4$ Spinel, *J. Electrochem. Soc.* 146 (1999) 857–861.
- [13] Y. Gu, K. Taniguchi, R. Tajima, S. Nishimura, D. Hashizume, A. Yamada, H. Takagi, A new “zero-strain” material for electrochemical lithium insertion, *J. Mater. Chem. A* 1 (2013) 6550. doi:10.1039/c3ta10878c.
- [14] A. Nakamura, Y. Gu, K. Taniguchi, N. Shibata, H. Takagi, Y. Ikuhara, Phase Interface Structures in $\text{Li}_{1+x}\text{Rh}_2\text{O}_4$ Zero Strain Cathode Material Analyzed by Scanning Transmission Electron Microscopy, *Chem. Mater.* 27 (2015) 938–943. doi:10.1021/cm5042106.
- [15] P. Liao, J. Li, J.R. Dahn, Lithium Intercalation in LiFe_2F_6 and LiMgFeF_6 Disordered Trirutile-Type Phases, *J. Electrochem. Soc.* 157 (2010) A355. doi:10.1149/1.3294788.
- [16] G. Lieser, C. Dräger, M. Schroeder, S. Indris, L. de Biasi, H. Geßwein, S. Glatthaar, H. Ehrenberg, J.R. Binder, Sol-Gel Based Synthesis of LiNiFeF_6 and Its Electrochemical Characterization, *J. Electrochem. Soc.* 161 (2014) A1071–A1077.
- [17] G. Lieser, L. de Biasi, H. Geßwein, S. Indris, C. Dräger, M. Schroeder, S. Glatthaar, H. Ehrenberg, J.R. Binder, Electrochemical Characterization of LiMnFeF_6 for Use as Positive Electrode in Lithium-Ion Batteries, *J. Electrochem. Soc.* 161 (2014) A1869–A1876.
- [18] L. de Biasi, G. Lieser, J. Rana, S. Indris, C. Dräger, S. Glatthaar, R. Mönig, H. Ehrenberg, G. Schumacher, J.R. Binder, H. Geßwein, Unravelling the mechanism of lithium insertion into and extraction from trirutile-type LiNiFeF_6 cathode material for Li-ion batteries, *CrystEngComm* 17 (2015) 6163–6174. doi:10.1039/C5CE00989H.

- 1
2
3
4
5
6
7
8
9
10
11
12
13
14
15
16
17
18
19
20
21
22
23
24
25
26
27
28
29
30
31
32
33
34
35
36
37
38
39
40
41
42
43
44
45
46
47
48
49
50
51
52
53
54
55
56
57
58
59
60
61
62
63
64
65
- [19] W. Viebahn, Über quaternäre Fluoride LiMIIMIIIIF_6 , Habilitationsschrift, Eberhard-Karls-Universität, 1976.
- [20] C. Dräger, G. Lieser, L. de Biasi, S. Indris, H. Geßwein, S. Glatthaar, M. Hoffmann, H. Ehrenberg, J.R. Binder, A Comparative Study of the Electrochemical Properties of Trirutile-type Quaternary Lithium Transition Metal Fluorides LiMFeF_6 (M= Mg, Co, Ni), Submitted. (n.d.).
- [21] G. Lieser, C. Dräger, L. de Biasi, S. Indris, H. Geßwein, S. Glatthaar, M.J. Hoffmann, H. Ehrenberg, J.R. Binder, Direct synthesis of trirutile-type LiMgFeF_6 and its electrochemical characterization as positive electrode in lithium-ion batteries, *J. Power Sources*. 274 (2015) 1200–1207. doi:10.1016/j.jpowsour.2014.10.151.
- [22] R.W. Cheary, A.A. Coelho, J.P. Cline, Fundamental Parameters Line Profile Fitting in Laboratory Diffractometers, *J. Res. Natl. Inst. Stand. Technol.* 109 (2004) 1–25.
- [23] D. Balzar, H. Ledbetter, Voigt-Function Modeling in Fourier Analysis of Size- and Strain-Broadened X-ray Diffraction Peaks, *J. Appl. Crystallogr.* 26 (1993) 97–103.
- [24] D. Balzar, N. Audebrand, M.R. Daymond, A. Fitch, A. Hewat, J.I. Langford, A. Le Bail, D. Louër, O. Masson, C.N. McCowan, N.C. Popa, P.W. Stephens, B.H. Toby, Size–strain line-broadening analysis of the ceria round-robin sample, *J. Appl. Crystallogr.* 37 (2004) 911–924. doi:10.1107/S0021889804022551.
- [25] K. Momma, F. Izumi, *VESTA 3* for three-dimensional visualization of crystal, volumetric and morphology data, *J. Appl. Crystallogr.* 44 (2011) 1272–1276. doi:10.1107/S0021889811038970.
- [26] S. Brunauer, P.H. Emmett, E. Teller, Adsorption of Gases in Multimolecular Layers, *Adsorpt. Gases Multimolecular Layers*. 60 (1938) 309–319.
- [27] P. Thompson, D.E. Cox, J.B. Hastings, Rietveld refinement of Debye–Scherrer synchrotron X-ray data from Al_2O_3 , *J. Appl. Crystallogr.* 20 (1987) 79–83.

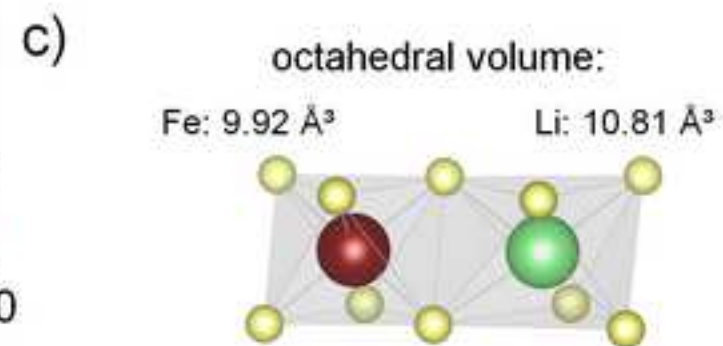
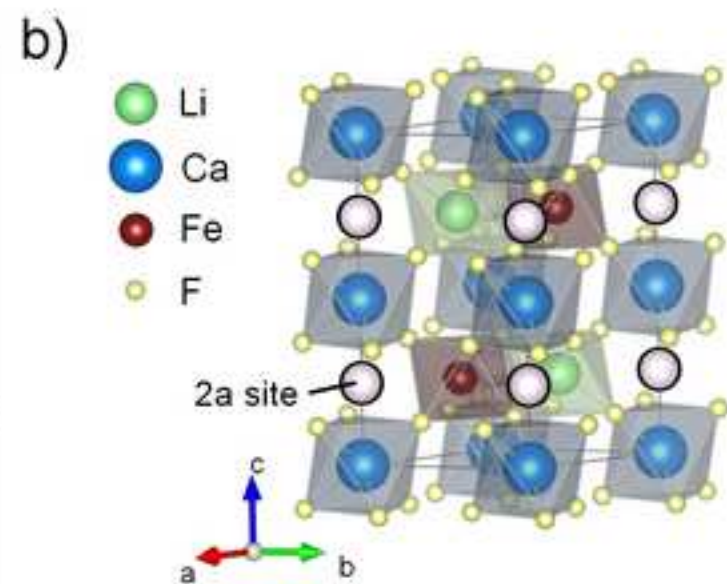
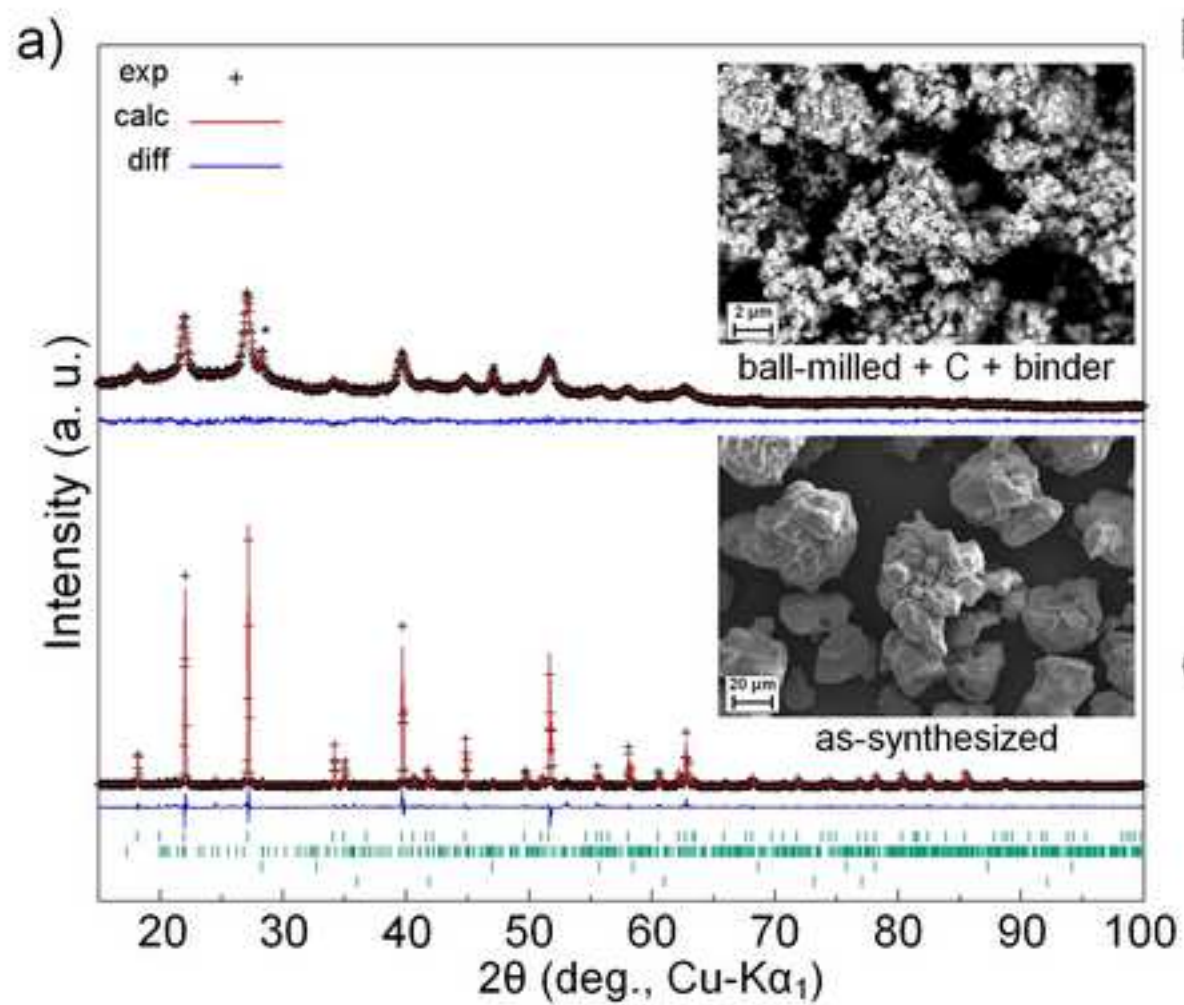
- 1
2
3
4
5
6
7
8
9
10
11
12
13
14
15
16
17
18
19
20
21
22
23
24
25
26
27
28
29
30
31
32
33
34
35
36
37
38
39
40
41
42
43
44
45
46
47
48
49
50
51
52
53
54
55
56
57
58
59
60
61
62
63
64
65
- [28] P. Norby, Synchrotron powder diffraction using imaging plates: crystal structure determination and Rietveld refinement, *J. Appl. Crystallogr.* 30 (1997) 21–30.
- [29] S.D. Kelly, D. Hesterberg, B. Ravel, Analysis of soils and minerals using X-ray absorption spectroscopy, *Methods Soil Anal. Part. 5* (2008) 387–463.
- [30] B. Ravel, M. Newville, *ATHENA*, *ARTEMIS*, *HEPHAESTUS*: data analysis for X-ray absorption spectroscopy using *IFEFFIT*, *J. Synchrotron Radiat.* 12 (2005) 537–541.
doi:10.1107/S0909049505012719.
- [31] W. Viebahn, Untersuchungen an quaternären Fluoriden LiMeII MeIII F_6 Die Struktur von LiCaAlF_6 , *Z. Für Anorg. Allg. Chem.* 386 (1971) 335–339.
- [32] P. Liao, R.A. Dunlap, J.R. Dahn, In Situ Mössbauer Effect Study of Lithium Intercalation in LiFe_2F_6 , *J. Electrochem. Soc.* 157 (2010) A1080.
doi:10.1149/1.3473809.
- [33] G. Lieser, M. Schroeder, H. Geßwein, V. Winkler, S. Glatthaar, M. Yavuz, J.R. Binder, Sol–gel processing and electrochemical characterization of monoclinic Li_3FeF_6 , *J. Sol-Gel Sci. Technol.* 71 (2014) 50–59. doi:10.1007/s10971-014-3329-1.
- [34] G. Lieser, L. de Biasi, M. Scheuermann, V. Winkler, S. Eisenhardt, S. Glatthaar, S. Indris, H. Geßwein, M.J. Hoffmann, H. Ehrenberg, J.R. Binder, Sol-Gel Processing and Electrochemical Conversion of Inverse Spinel-Type Li_2NiF_4 , *J. Electrochem. Soc.* 162 (2015) A679–A686.
- [35] G. Lieser, V. Winkler, H. Geßwein, L. de Biasi, S. Glatthaar, M.J. Hoffmann, H. Ehrenberg, J.R. Binder, Electrochemical characterization of monoclinic and orthorhombic Li_3CrF_6 as positive electrodes in lithium-ion batteries synthesized by a sol–gel process with environmentally benign chemicals, *J. Power Sources.* 294 (2015) 444–451. doi:10.1016/j.jpowsour.2015.06.036.
- [36] C.P. Grey, N. Dupré, NMR Studies of Cathode Materials for Lithium-Ion Rechargeable Batteries, *Chem. Rev.* 104 (2004) 4493–4512. doi:10.1021/cr020734p.

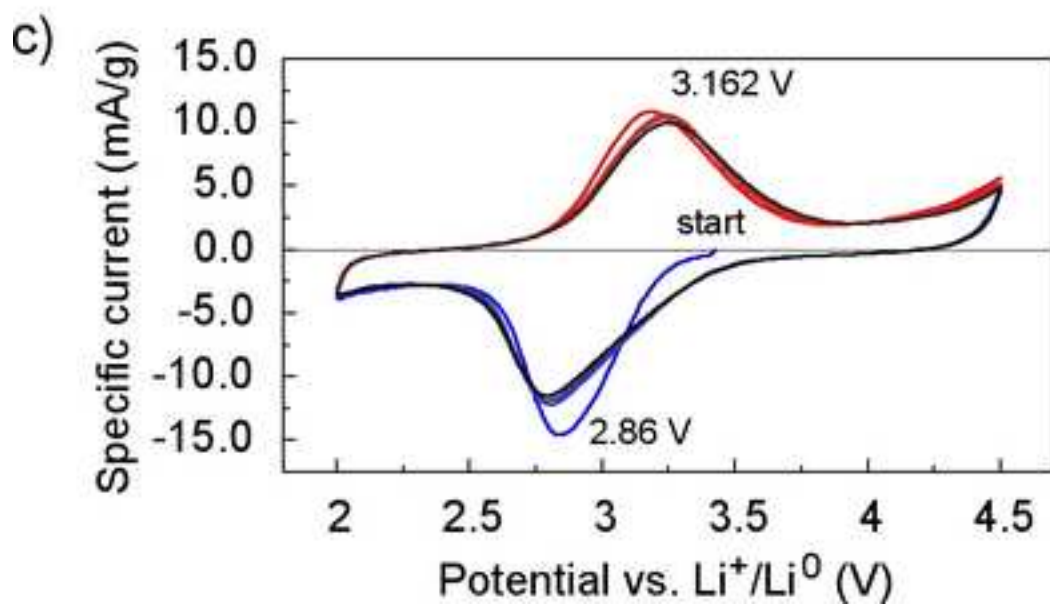
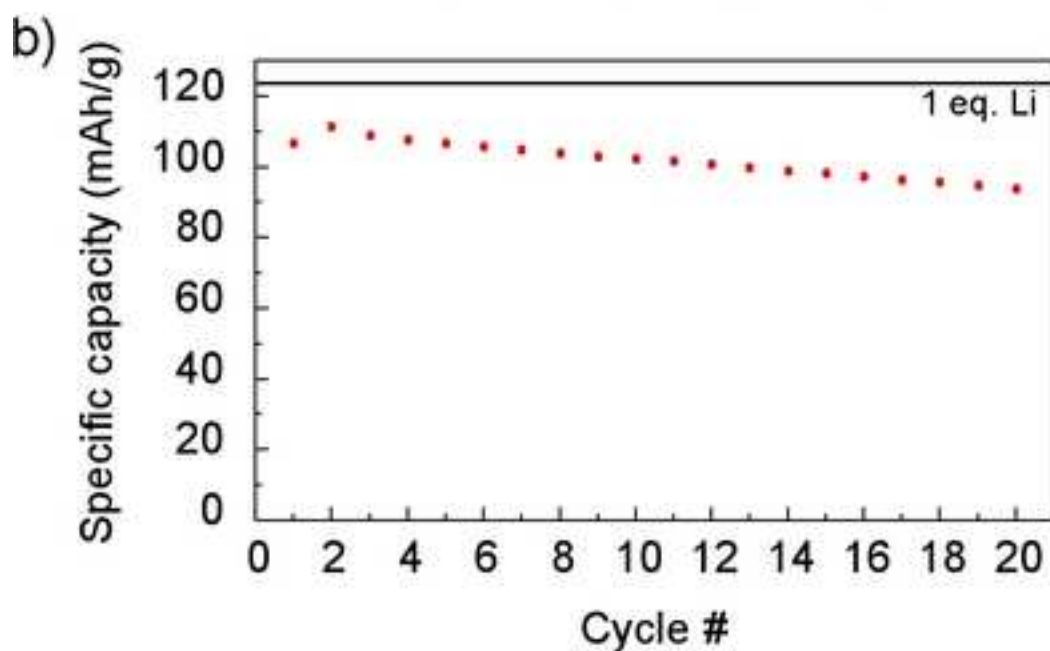
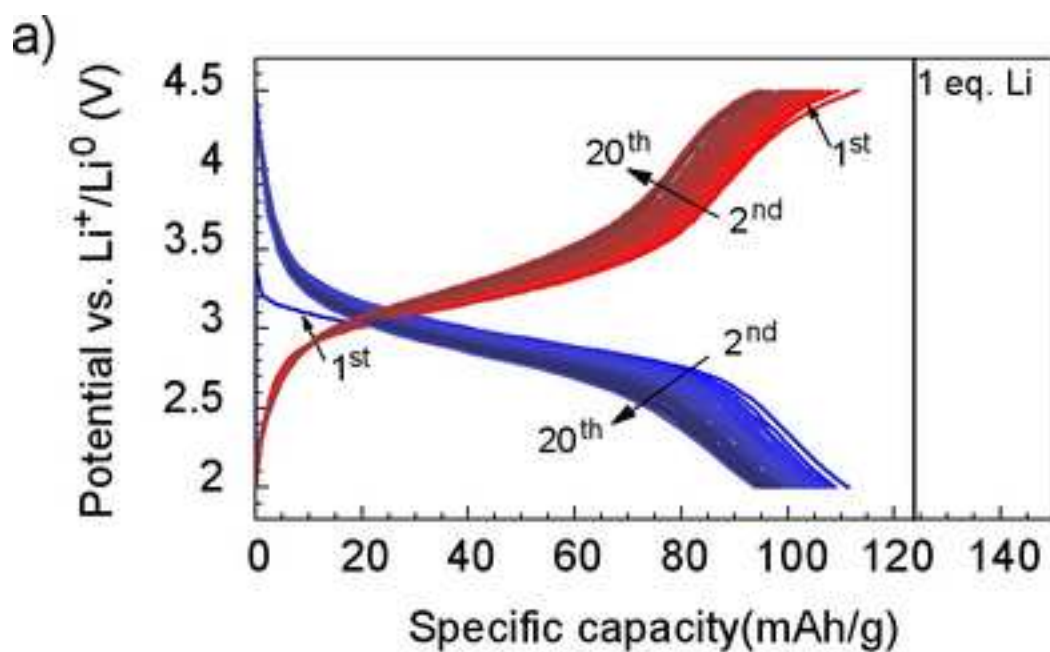
- 1
2
3
4
5
6
7
8
9
10
11
12
13
14
15
16
17
18
19
20
21
22
23
24
25
26
27
28
29
30
31
32
33
34
35
36
37
38
39
40
41
42
43
44
45
46
47
48
49
50
51
52
53
54
55
56
57
58
59
60
61
62
63
64
65
- [37] R. Chen, R. Heinzmann, S. Mangold, V.S.K. Chakravadhanula, H. Hahn, S. Indris, Structural Evolution of $\text{Li}_2\text{Fe}_{1-y}\text{Mn}_y\text{SiO}_4$ ($y = 0, 0.2, 0.5, 1$) Cathode Materials for Li-Ion Batteries upon Electrochemical Cycling, *J. Phys. Chem. C.* 117 (2013) 884–893. doi:10.1021/jp310935j.
- [38] I. Bezza, M. Kaus, R. Heinzmann, M. Yavuz, M. Knapp, S. Mangold, S. Doyle, C.P. Grey, H. Ehrenberg, S. Indris, I. Saadoune, Mechanism of the Delithiation/Lithiation Process in $\text{LiFe}_{0.4}\text{Mn}_{0.6}\text{PO}_4$: in Situ and ex Situ Investigations on Long-Range and Local Structures, *J. Phys. Chem. C.* 119 (2015) 9016–9024. doi:10.1021/jp513032r.
- [39] T. Yamamoto, Assignment of pre-edge peaks in K-edge x-ray absorption spectra of 3d transition metal compounds: electric dipole or quadrupole?, *X-Ray Spectrom.* 37 (2008) 572–584. doi:10.1002/xrs.1103.
- [40] A. Yamada, S.-C. Chung, Crystal Chemistry of the Olivine-Type $\text{Li}(\text{Mn}_{1-y}\text{Fe}_y)\text{PO}_4$ and $(\text{Mn}_y\text{Fe}_{1-y})\text{PO}_4$ as Possible 4 V Cathode Materials for Lithium Batteries, *J. Electrochem. Soc.* 148 (2001) A960. doi:10.1149/1.1385377.
- [41] M. Pouchard, A. Villesuzanne, J.-P. Doumerc, Spin State Behavior in Some Cobaltites (III) and (IV) with Perovskite or Related Structure, *J. Solid State Chem.* 162 (2001) 282–292. doi:10.1006/jssc.2001.9294.
- [42] P. Tang, N.A.W. Holzwarth, Electronic structure of FePO_4 , LiFePO_4 , and related materials, *Phys. Rev. B.* 68 (2003). doi:10.1103/PhysRevB.68.165107.
- [43] A. Deb, U. Bergmann, S.P. Cramer, E.J. Cairns, Structural investigations of LiFePO_4 electrodes and in situ studies by Fe X-ray absorption spectroscopy, *Electrochimica Acta.* 50 (2005) 5200–5207. doi:10.1016/j.electacta.2005.02.086.
- [44] T. Ohzuku, A. Ueda, Solid-State Redox Reactions of LiCoO (R3m) for 4 Volt Secondary Lithium Cells, *J. Electrochem. Soc.* 141 (1994) 2972–2977.

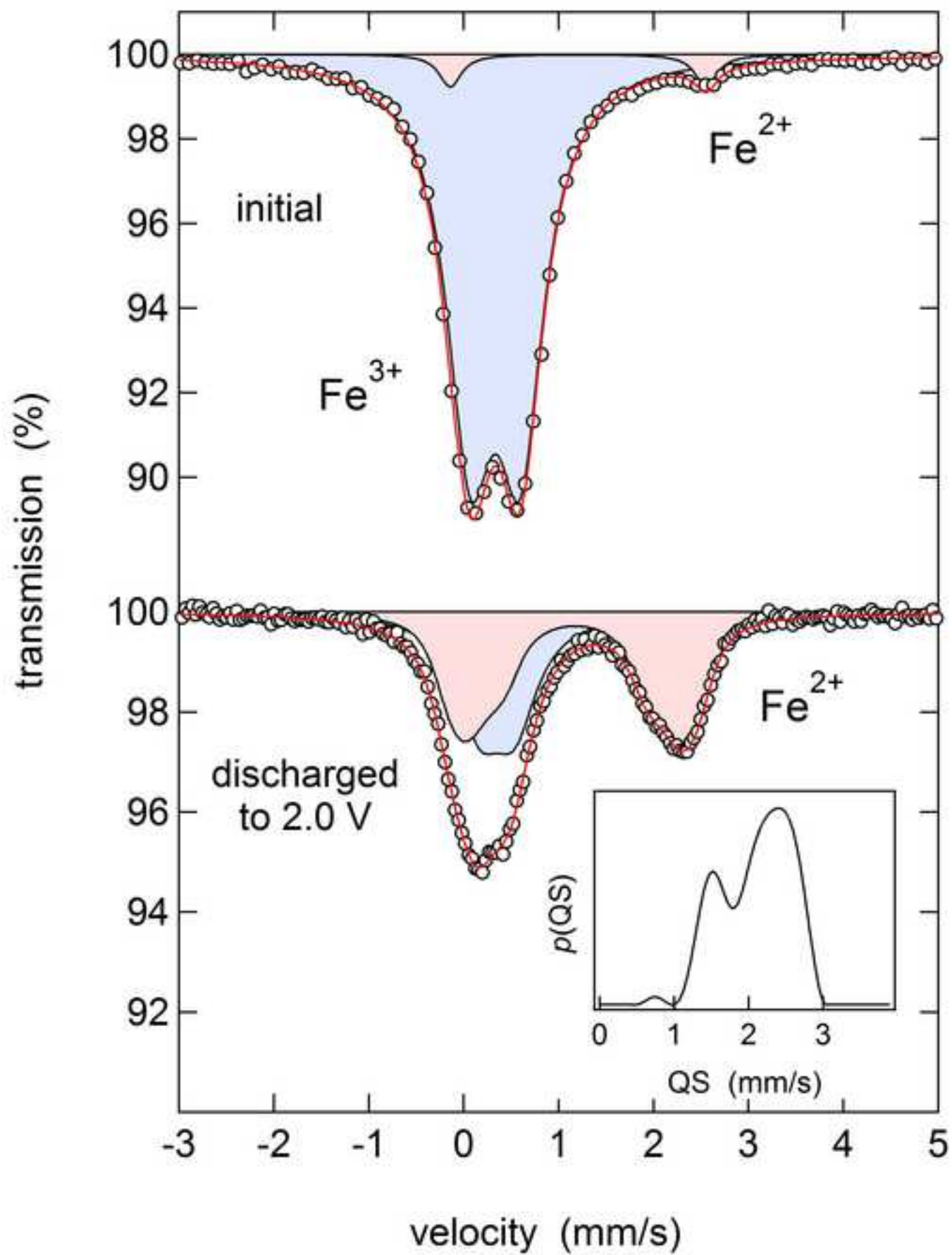
- 1
2
3
4
5
6
7
8
9
10
11
12
13
14
15
16
17
18
19
20
21
22
23
24
25
26
27
28
29
30
31
32
33
34
35
36
37
38
39
40
41
42
43
44
45
46
47
48
49
50
51
52
53
54
55
56
57
58
59
60
61
62
63
64
65
- [45] N. Yabuuchi, T. Ohzuku, Novel lithium insertion material of $\text{LiCo}_{1/3}\text{Ni}_{1/3}\text{Mn}_{1/3}\text{O}_2$ for advanced lithium-ion batteries, *J. Power Sources*. 119-121 (2003) 171–174.
doi:10.1016/S0378-7753(03)00173-3.
- [46] D.A. Pawlak, K. Wozniak, K. Shimamura, T. Fukuda, Correlation between structural parameters of colquiriite structures, *J. Cryst. Growth*. 233 (2001) 699–708.
- [47] J. Galy, S. Andersson, Some proposals for transformation mechanisms of the Li_2ZrF_6 , trirutile and Na_2SiF_6 structure types: Simple cation rearrangements, *J. Solid State Chem.* 3 (1971) 525–528.
- [48] R.D. Shannon, Revised effective ionic radii and systematic studies of interatomic distances in halides and chalcogenides, *Acta Crystallogr. A*. 32 (1976) 751–767.

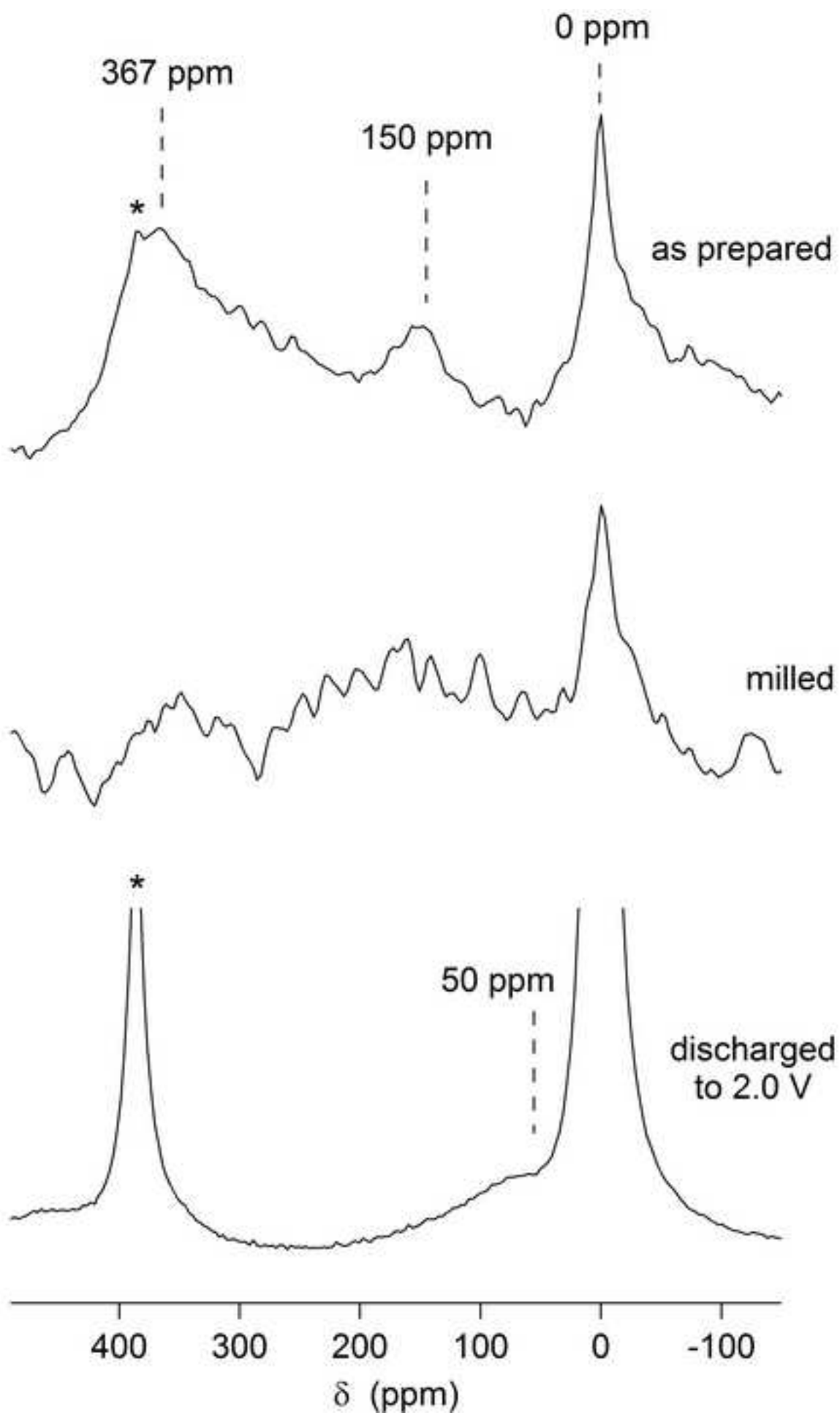
Table 1

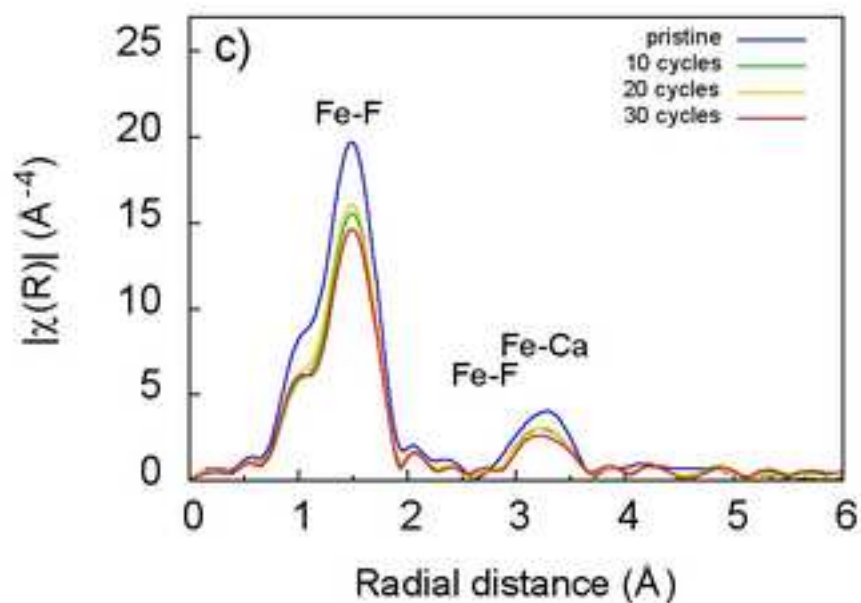
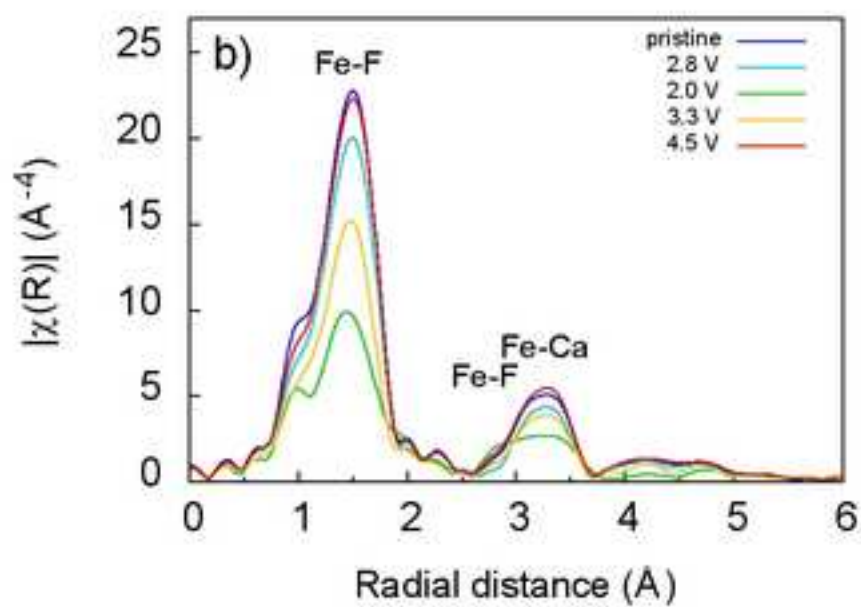
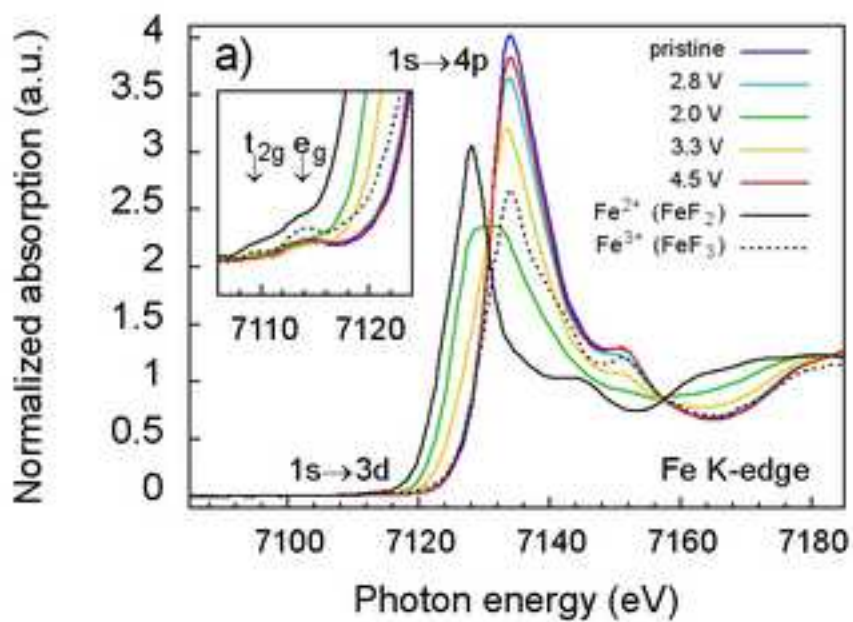
Sample	a (Å)	c (Å)		Vol (Å ³)		
As-synthesized	5.1299(1)	9.7765(2)		222.80(1)		
Ball-milled	5.1336(11)	9.7791(29)		223.2(2)		
1 st discharge (2.0 V)	5.1414(7)	9.80128(210)		224.4(1)		
1 st charge (4.5 V)	5.1366(7)	9.78576(214)		223.6(1)		
2 nd discharge (2.0 V)	5.1408(7)	9.8030(21)		224.3(1)		
Atom	Wyckoff	x	y	y	occ	B _{eq}
Ca	2b	0	0	0	1	0.72(9)
Li	2c	1/3	2/3	1/4	1	1.00
Fe	2d	2/3	1/3	1/4	1	0.45(6)
F (as-synthesized)	12i	0.3649(9)	0.0137(7)	0.1378(3)	1	1.34(9)
F (ball-milled)	12i	0.3573(21)	0.0093(9)	0.1392(6)	1	1.34(9)
F (discharged)	12i	0.3622(15)	0.0137(7)	0.1328(6)	1	1.34(9)



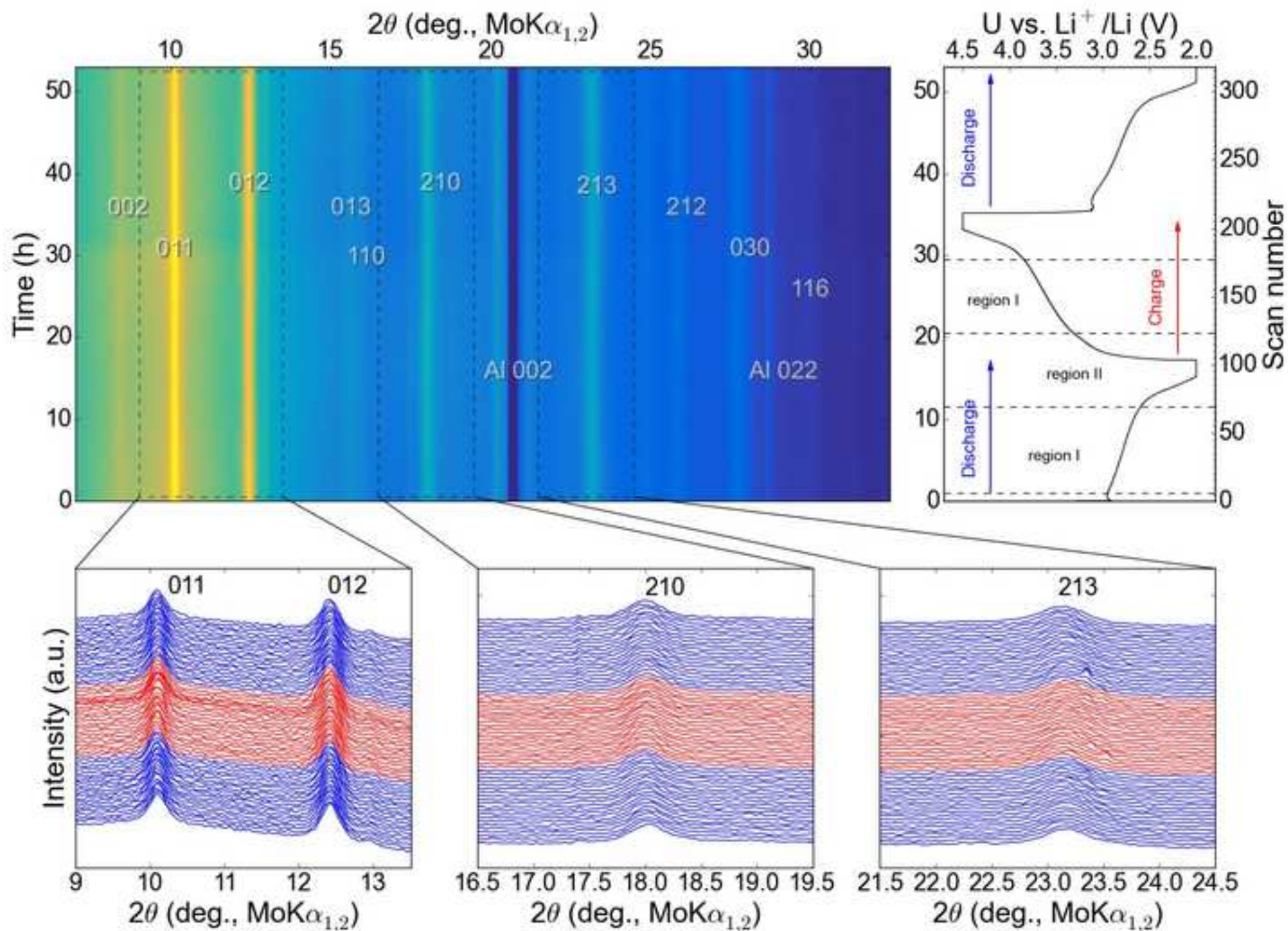


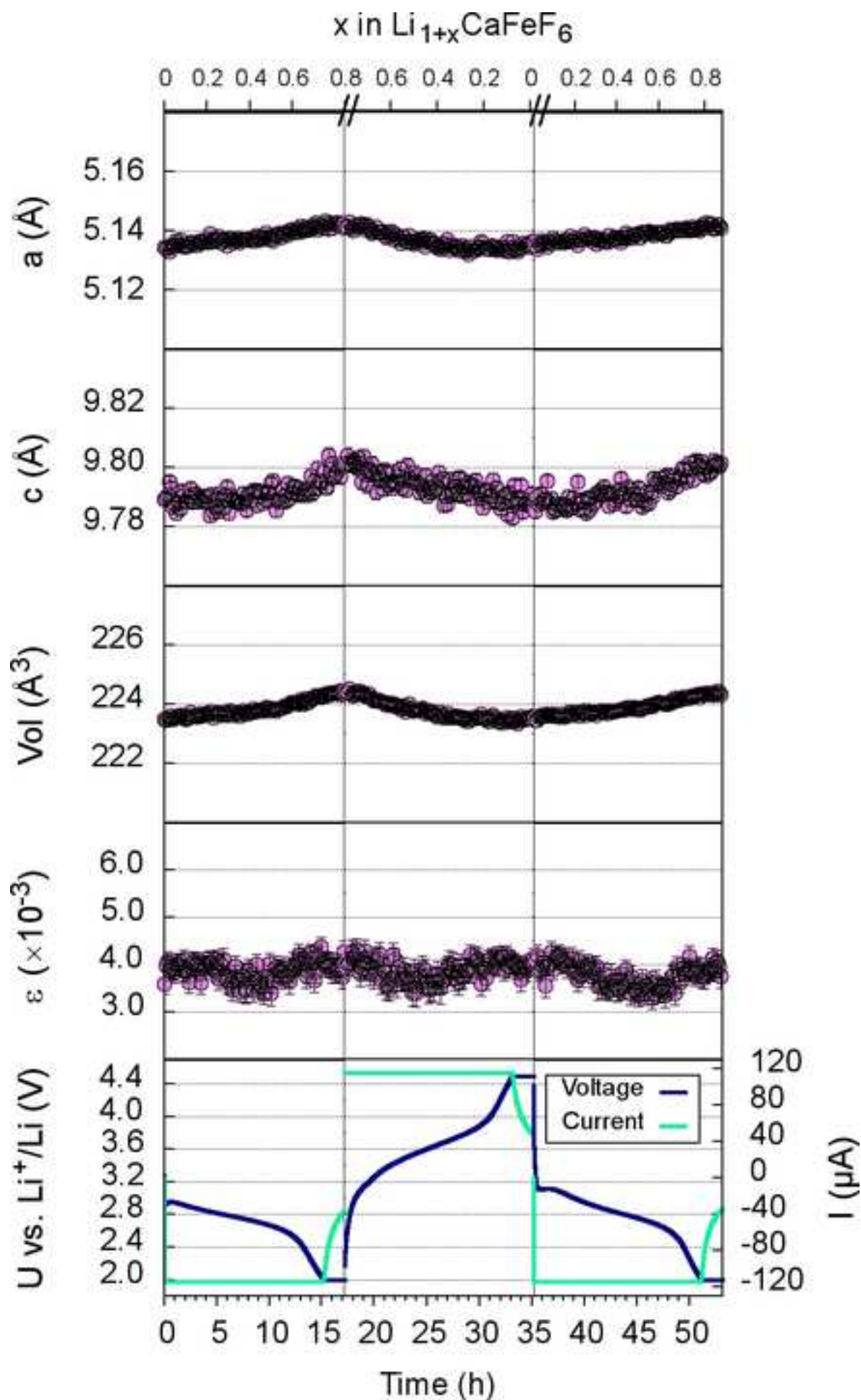






Figure(s) - provide separately in addition to within the manuscript file
[Click here to download high resolution image](#)





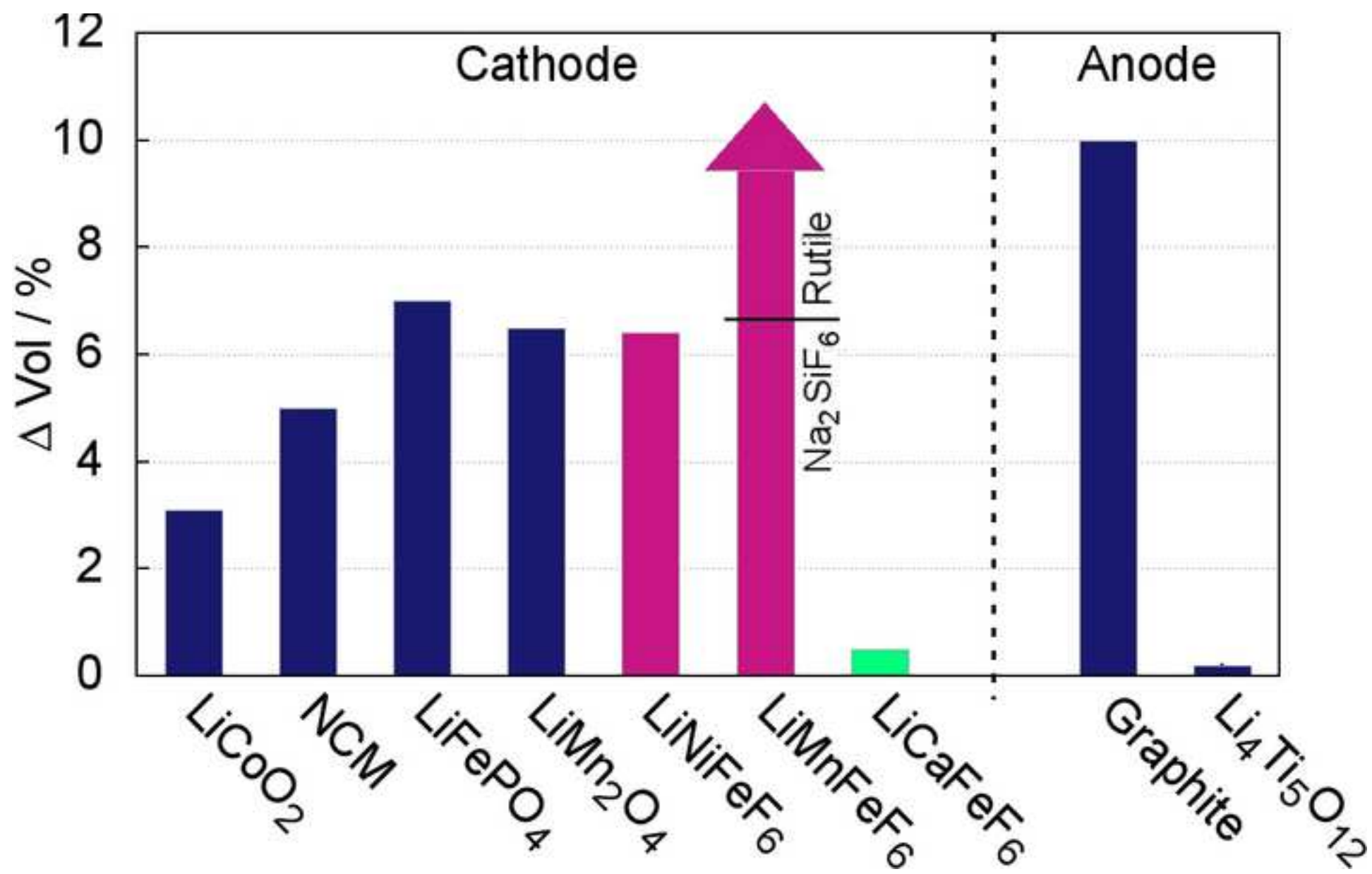


Figure captions

Fig. 1: a) Powder X-ray diffraction patterns and SEM micrographs of the as-synthesized LiCaFeF_6 (bottom) and after ball-milling with carbon and PVDF binder (top). Green ticks mark the positions of reflections of LiCaFeF_6 and impurity phases Li_3FeF_6 , CaF_2 , and LiF (from top to bottom). Asterisks mark CaF_2 impurity reflections in the ball-milled composite. b) Colquiriite-type crystal structure of LiCaFeF_6 with empty 2a site that is suggested for the insertion of additional lithium. c) The large ionic radius of initial Li^+ -ions, which are present in the pristine crystal structure, and the associated high $[\text{LiF}_6]$ -octahedral volume stabilize the interlayer distance between $[\text{CaF}]$ -layers.

Fig. 2: a) Discharge (blue) and charge (red) profiles at galvanostatic cycling of $\text{LiCaFeF}_6/\text{C}$ composite cathode at a rate of C/20. b) Discharge capacity of the $\text{LiCaFeF}_6/\text{C}$ composite cathode during galvanostatic cycling at a rate of C/20. c) Slow-scan cyclic voltammetry ($20 \mu\text{V s}^{-1}$) of the $\text{LiCaFeF}_6/\text{C}$ composite cathode within the potential range from 2.0 to 4.5 V.

Fig. 3: ^{57}Fe Mössbauer spectra of LiCaFeF_6 in the as-prepared state and after discharging to 2.0 V. The experimental data points are given as white circles and the fits are given as red lines. Fe^{3+} and Fe^{2+} subspectra are given as blue and red doublets, respectively. The inset shows the distribution of quadrupole splittings used to describe the Fe^{2+} doublet after discharging to 2.0 V.

Fig. 4: ^7Li MAS NMR spectra of LiCaFeF_6 directly after synthesis, after milling with PVDF and carbon, and after discharging against Li metal down to 2.0 V. Spinning sidebands are marked with an asterisk.

Fig. 5: Normalised X-ray absorption spectra (a) and Fourier transforms of the k^3 -weighted EXAFS signals $X(k)$ (b) at the Fe K-edge of $\text{Li}_{1+x}\text{CaFeF}_6$ measured in the pristine state ($\text{Li}_{1.00}\text{CaFeF}_6$) and *ex situ* after cycling to various electrochemical states of discharge (2.8 V ($\text{Li}_{1.42}\text{CaFeF}_6$), 2.0 V ($\text{Li}_{1.77}\text{CaFeF}_6$)) and charge (3.3 V ($\text{Li}_{1.42}\text{CaFeF}_6$), 4.5 V ($\text{Li}_{1.00}\text{CaFeF}_6$)). Further spectra are measured in the charged state at 4.5 V after cycling over a period of 10, 20, and 30 cycles (c). Labels of peaks in the Fourier transforms assign the coordination shell. The inset in (a) shows an expanded view of the pre-edge region.

Fig. 6: Evolution of *in situ* X-ray diffraction patterns of LiCaFeF_6 during the first three half-cycles.

Fig. 7: Rietveld refinement results of lattice metric and microstrain of LiCaFeF_6 as a function of Li content electrochemical state.

Fig. 8: Comparison of the relative volume change of LiCaFeF_6 cathode material with that of other quaternary $\text{LiMe}^{\text{II}}\text{FeF}_6$ compounds [17,18] as well as with that of commercially used electrode materials [1,4,11,44,45].

Table captions

Table 1: Lattice parameters and unit cell volume of LiCaFeF_6 directly after synthesis, after ball-milling and after cycling. Atomic coordinates from Rietveld refinement and isotropic thermal displacement parameters (B_{eq} of Li is taken from literature [31]) of LiCaFeF_6 after synthesis, after ball-milling and in the discharged state ($\text{Li}_{1.79}\text{CaFeF}_6$; determined by *ex situ* XRD).

Supplementary Materials

[Click here to download Supplementary Materials: Supporting_Information.docx](#)